DIOGO ALEXANDRE INÁCIO AMARO

BSc in Biomedical Engineering

STATISTICAL EMULATION OF COMPLEX CARDIAC MODELS USING GAUSSIAN PROCESSES

MASTER IN BIOMEDICAL ENGINEERING

NOVA University Lisbon
September, 2025

STATISTICAL EMULATION OF COMPLEX CARDIAC MODELS USING GAUSSIAN PROCESSES

DIOGO ALEXANDRE INÁCIO AMARO

BSc in Biomedical Engineering

Adviser: Dr. Hao Gao
Senior Lecturer, University of Glasgow

Co-adviser: Prof. Dr. Ricardo Nuno Pereira Verga e Afonso Vigário
Associate Professor, NOVA University Lisbon

Statistical Emulation of Complex Cardiac Models Using Gaussian Processes

To my parents and my brother.

Acknowledgements

I would like to begin by expressing my sincere gratitude to my advisor, Dr. Hao Gao, who welcomed me into his supervision and always made himself available to assist me during my project. It has been a true honor to work with someone whose many years of research in this field I deeply admire and aspire to. His guidance has been fundamental to the completion of this thesis, and I will always remain grateful for the support.

Secondly, I would like to give a special thanks to Prof. Ricardo Vigário, my co-advisor, who guided me into starting this journey one year ago. Beyond his role as co-advisor, I cannot help but express my gratitude for having been one of the best teachers I had throughout my five years at this University. The way complex topics were explained and progressively deconstructed during classes was truly impressive, and I am deeply thankful for that too.

I would also like to express my appreciation to FCT, in particular to the Department of Physics, and to all its professors, for the knowledge, training, and encouragement I received here, which have been crucial in shaping me both as a person and as an academic. I am especially grateful to Prof. Carla Quintão and, later, Prof. Célia Henriques, for their excellent work as academic coordinators of the Biomedical Engineering Integrated Master's degree. On numerous occasions, who many times faced administrative challenges with dilligence and care, ensuring that solutions were discussed and agreed upon with the students beforehand.

On a more personal note, I would like to express my deepest gratitude to my family, whose love, support, and encouragement have been the foundation of everything I have achieved. Particularly to my parents, Ana and Rui, for believing in me and trusting my personal judgment when hard decisions came by, and to my brother, Duarte, for the support over the years.

Finally, I want to thank my friends for being present throughout these years, and I hope we can preserve this friendship for many years to come.

"It is not knowledge, but the act of learning, not possession but the act of getting there, which grants the greatest enjoyment."

— **Carl Friedrich Gauss**, Letter to Bolyai (1808)
(Mathematician, astronomer, and physicist)

Abstract

Cardiovascular diseases remain the leading cause of mortality worldwide, and patient-specific cardiac computational models offer critical insights for diagnosis, prognosis, and the development of individualized treatment plans. The increasing sophistication of these models places them well beyond the reach of analytical solutions, demanding the use of numerical physics simulators to approximate physiological behavior.

Such models are typically governed by complex partial differential equations (PDEs), whose solution requires computationally intensive numerical methods, making them impractical for real-time clinical applications. An alternative approach which can help bypass these challenges is *emulation*, whereby the original simulator is replaced by a data-driven surrogate model.

This thesis explores the use of Gaussian Processes (GPs) as a statistical emulator for the passive diastolic filling of the left ventricle (LV), enabling fast approximation of model outputs from physiological input parameters.

We illustrate the principles of surrogate modelling using two toy examples. The first highlights the underlying mechanics of GPs by fitting a sinusoidal function, while the second adapts this mechanism to a simplified cardiac scenario. Building on this foundation, we construct statistical surrogates for six output features generated by a high-fidelity forward simulation of left ventricular dynamics. These emulators are then used to perform predictive modelling and validated by Sobol sensitivity analysis. Lastly, we use those to perform parameter inference, both from a deterministic and probabilistic point of view. Finally, we interpret the results and demonstrate via theoretical analysis and numerical experiments that cardiac mechanical models can be deployed for real-time clinical decision support.

Keywords: Left ventricular mechanics, statistical emulation, digital twin, Gaussian Processes, parameter inference, uncertainty quantification

The research work described in this dissertation was carried out in accordance with the norms established in the ethics code of Universidade Nova de Lisboa. The work described and the material presented in this dissertation, with the exceptions clearly indicated, constitute original work carried out by the author.

In the present work, generative artificial intelligence tools, namely ChatGPT 5, were used for grammatical revision, text reformulation, and adaptation of certain signal processing algorithms. These tools were employed under the supervision of the author, and all generated content was verified for accuracy. The authorship and validation of the content remain entirely the responsibility of the author, and the use of artificial intelligence complies with institutional standards of academic integrity.

Resumo

As doenças cardiovasculares continuam a ser a principal causa de mortalidade a nível mundial, e os modelos computacionais cardíacos específicos de cada paciente oferecem informações cruciais para o diagnóstico, prognóstico e desenvolvimento de planos de tratamento individualizados. A crescente sofisticação destes modelos coloca-os muito além do alcance de soluções analíticas, exigindo o recurso a simuladores numéricos de física para aproximar o comportamento fisiológico.

Estes modelos são tipicamente governados por complexas equações diferenciais parciais (EDP), cuja resolução requer métodos numéricos computacionalmente intensivos, tornando impraticável a sua utilização em aplicações clínicas em tempo real. Uma abordagem alternativa que pode ajudar a contornar estes obstáculos é a *emulação*, onde o simulador original é substituído por um modelo substituto, orientado por dados.

Esta dissertação explora a utilização de Processos Gaussianos (PGs) como emulador estatístico do enchimento diastólico passivo do ventrículo esquerdo (VE), permitindo uma aproximação rápida dos resultados do modelo a partir de parâmetros fisiológicos de entrada.

Ilustramos os princípios da modelação substituta através de dois exemplos simplificados. O primeiro destaca a mecânica subjacente dos PGs ao ajustar uma função sinusoidal, enquanto o segundo adapta esse mecanismo a um cenário cardíaco simplificado. A partir desta base, construímos modelos substitutos estatísticos para seis variáveis de saída geradas por uma simulação de alta fidelidade da dinâmica ventricular esquerda. Estes emuladores são depois utilizados para realizar modelação preditiva e validados por meio de uma análise de sensibilidade de Sobol. Por fim, aplicámo-los à inferência de parâmetros, tanto numa perspetiva determinística como probabilística. Finalmente, interpretamos os resultados e demonstramos por meio de uma análise teórica e de testes numéricos que modelos mecânicos cardíacos podem ser implementados para suporte a decisões clínicas em tempo real.

Palavras-chave: Mecânica do ventrículo esquerdo, emulação estatística, gémeo digital, Processos Gaussianos, inferência de parâmetros, quantificação de incerteza

CONTENTS

LIST OF TABLES

Acronyms

ANOVA   analysis of variance *(p. 26)*

CT   computed tomography *(p. 30)*

DE   differential evolution *(pp. xi, 32, 33)*
DTI   diffusion tensor imaging *(p. 4)*

EDP   equações diferenciais parciais *(p. vii)*
EDV   end diastolic volume *(p. 21)*

FEM   finite element method *(p. 22)*

GP   Gaussian Process *(pp. xi, 14, 16–24, 34, 38, 40)*
GPR   Gaussian Process regression *(pp. 1, 19, 21, 23, 40)*
GPs   Gaussian Processes *(pp. v, 38, 40)*
GSA   global sensitivity analysis *(pp. 26–30)*

KNN   K-nearest neighbors *(p. 24)*

LSA   local sensitivity analysis *(pp. 26, 28–30)*
LV   left ventricle *(pp. v, viii, x, xi, 1, 2, 4–6, 8–12, 21, 22, 24, 26, 28, 30–32, 34, 36, 38–40)*

MAP   maximum a posteriori *(pp. 34, 35, 37)*
MCMC   Markov chain Monte Carlo *(p. 31)*
MLP   multi-layer perceptron *(p. 24)*
MRI   magnetic resonance imaging *(p. 30)*
MS   mean-squared *(p. 17)*
MSE   mean squared error *(pp. 25, 32, 37)*

Introduction

Cardiovascular disease remains the leading cause of mortality worldwide, accounting for nearly one third of global deaths each year [2]. Therefore, early diagnosis and patient-specific risk stratification are central challenges in modern medicine. Mathematical modelling of the heart has emerged as a research area, as it promises to substantially advance early diagnosis of ventricular dysfunction and risk of myocardial infarction. Accurate simulations of cardiac dynamics could, in principle, support diagnosis and guide clinical decision-making by predicting the mechanical response of the myocardium under different conditions.

Despite this potential, high-fidelity simulations are rarely used in clinical workflows due to their computational cost. Finite element models of cardiac mechanics rely on complex PDEs solved numerically on three-dimensional meshes, making a single simulation last hours or days, even on high-performance computing resources. Such requirements are incompatible with clinical practice, where fast and repeated evaluation is necessary.

A promising way forward is *statistical emulation*. Instead of solving the full system of equations for every new input, emulators approximate the input–output relationship using a data-driven surrogate model. Gaussian Process regression (GPR) offers a principled Bayesian framework for this purpose, as it captures nonlinear dependencies, quantifies uncertainty, and can be trained on relatively few simulations. Essentially, the idea is to approximate the computationally expensive mathematical model (the simulator) with a computationally cheap statistical surrogate model (the emulator) by a combination of massive parallelization and nonlinear regression, so as to exploit computational resources before the patient arrives at the clinic.

In this thesis, we construct and validate a statistical emulator for the mechanics of the LV during diastolic filling. First, we generate a dataset of finite element simulations using a reduced set of material parameters. Second, we train Gaussian Process emulators to approximate the mapping between parameters and biomechanical outputs. Finally, we employ the trained emulator to solve inverse problems through deterministic global optimization and Bayesian inference, demonstrating its potential to recover cardiac parameters from observed data, otherwise accessible only through invasive procedures.

Biomechanical Model of LV Dynamics

This chapter introduces the biomechanical model that describes the behaviour of the LV during diastole, which is the focus of the analysis in the remainder of this thesis. An overview of cardiac anatomy is first provided before considering the LV in more detail. In order to accurately study myocardial constitutive behaviour, multiple physiological aspects must be studied and taken into consideration before developing a modelling framework that integrates detailed measures of the LV. In particular, four components are essential for constructing a realistic representation of LV mechanics: (i) LV geometry and fibre architecture, (ii) myocardial kinematics, (iii) physiological boundary and loading conditions, and (iv) constitutive laws describing the nonlinear, anisotropic stress–strain response of the myocardium.

2.1 Mechanical Behaviour of the Passive Myocardium

2.1.1 The Heart

The human heart is an ellipsoidal hollow organ that pumps blood into the arteries of the systemic and pulmonary circulations and collects it after its return through the veins [3]. Specifically, it supplies oxygenated blood and nutrients to the body's network of cells through arteries, while simultaneously collecting deoxygenated blood from the veins and sending it to the lungs for reoxygenation.

The heart is divided into left and right sides, each containing two chambers: an atrium and a ventricle. The interatrial and interventricular septa separate the left and right hearts, preventing direct blood transfer between them. While the atria receive blood, the ventricles are responsible for pumping it out. The LV is particularly notable, as it has the largest volume among the four chambers and must generate significantly higher pressure to distribute blood throughout the entire body. As a consequence of the need to support higher pressures, its walls are considerably thicker ($\approx$10 mm in adults) compared to the right ventricle (RV), whose free wall is typically 3–4 mm thick and generates roughly one-fifth of the pressure of the LV [4].

Blood flow within the heart is precisely controlled by four valves. The atrioventricular

valves connect the atria to the ventricles through the tricuspid valve on the right side, and the mitral valve on the left. Two additional valves, the aortic valve (left side) and the pulmonary valve (right side), separate the ventricles from the circulatory system. Notably, no valves are present between the atria and their corresponding terminal veins (see Figure 2.1).

The heart wall itself consists of three distinct layers. The endocardium is the thin, internal layer that lines the inside of all four chambers. This serous membrane, approximately 100 μm thick, is primarily composed of epimysial collagen, elastin, and a layer of endothelial cells that serve as an interface with the blood. The middle, and comparatively thick, muscular layer is the myocardium. The myocardium of the left ventricle is almost twice as thick as that of the right ventricle, reflecting its greater workload. The outermost thin layer is the epicardium, also a protective membrane around 100 μm thick, made of epimysial collagen and some elastin. Surrounding the epicardium is the pericardium, another serous membrane that isolates the heart from adjacent organs and facilitates its movements. While there's ongoing debate regarding the heart's microstructure [5–7], some describe it as a single muscle coiled helically, others as a continuum of laminar sheets. Nevertheless, it's widely recognized that myocardial fibres exhibit a clear preferred orientation, crucial for the scope of this work.
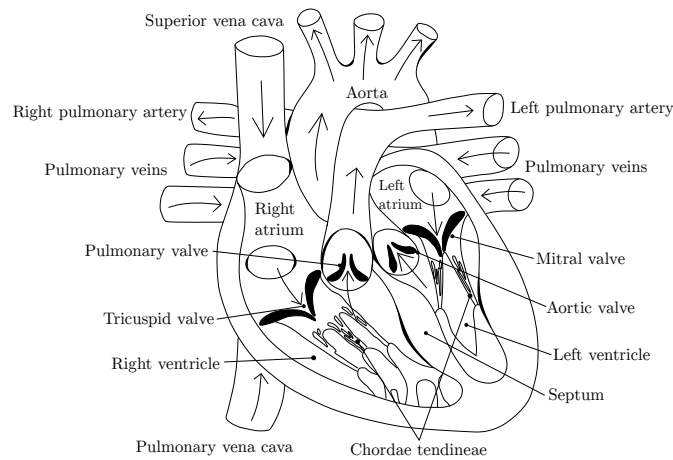
Figure 2.1: Anatomical overview of the human heart. The figure illustrates the four chambers (left and right atria, left and right ventricles), the major valves (tricuspid, mitral, pulmonary, and aortic), and the main inflow and outflow vessels. The arrows indicate the direction of blood flow through the heart and into the systemic and pulmonary circulations.

2.1.2 Myofibre Architecture

The myocardium, made up of a series of myofibres which, in turn, are made up of a series of functional units called myocytes, exhibits an anisotropic behaviour, critical to its electrical and mechanical function [8]. Kumar et al. defined the structural architecture of the muscle fibres as one of the most important factors to healthy pump function [9].

3

In fact, many cardiac disorders or traumatic events induce cardiac fibre misalignment, which may cyclically reduce cardiac function and lead to further disorganization [10]. Previous studies, particularly diffusion tensor imaging (DTI), have shown that myofibres are arranged in a highly layered architecture, rotating continuously from endocardial to epicardial surfaces [11]. A rule based method is used to describe the myofibre structure by defining a local material coordinate system fibre (**f**)-sheet (**s**)-normal (**n**) [12], where myofibres (**f**) are assumed to rotate transmurally from -60° in the endocardial surface to +60° in the epicardial surface [13, 14]. These myofibres reside within sheets (laminae) connected by shear layers, forming a sheet plane, which is orthogonal to **f**. A unit vector within the sheet plane is then defined, **s**, for the sheet direction and rotates from -45° to 45° from endocardium to epicardium. Accordingly, **n** is the sheet-normal. A schematic representation of this coordinate system is shown in Figure 2.2.
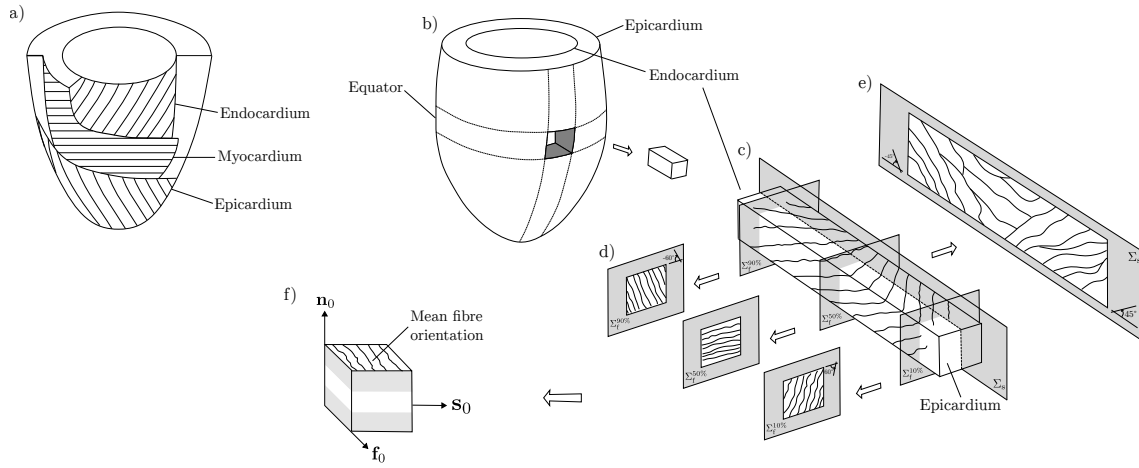
Figure 2.2: Representation of: (a) the anterior view of the LV, with the corresponding layers and fibre orientation associated with each layer; (b) the LV and a cutout from the equator; (c) the block taken from the equatorial site; (d) three longitudinal–circumferential sections at regular intervals from 10% to 90%, each described by a surface $\sum_f^{p\%}$, of the wall thickness from the epicardium showing the transmural variation of fibre orientation from -60° at the endocardium to +60° at the epicardium. (e) one transmural LV wall cross-section showing the continuous rotation of sheet orientation from -45° at the endocardium to +45° at the epicardium and described by its surface $\sum_s$; (f) a cube of myocardial tissue illustrating layered architecture and local material axes (X_1, X_2, X_3), which serve as the reference basis for both geometrical description and constitutive modelling. Adapted from [15, 16].

Moreover, the transmural fibre rotation is not only crucial to the anisotropic mechanical properties of the myocardium, but it is also the root of the intrinsic torsional motion of the LV. During the cardiac cycle, the apex and base of the heart rotate in opposite directions. This behaviour is caused by the specific layering of fibres. In the LV, fibres in the subepicardium run in a left-handed direction, fibres in the mid layer run circumferentially, and fibres in the (sub)endocardium run in a right-handed direction [17]. Because these fibre groups are actively connected and activated together, their contraction leads not only

to radial and longitudinal deformation, but also to a net rotational effect [18].

While the present work focuses on the passive filling phase, and does not explicitly simulate the torsion mechanism of the LV, it is still important to have a context of this mechanism, mainly because of two reasons. Firstly, from a physiological standpoint, it is well defined that the degree of shortening of myocardial fibres is of the order of 15-20%, at most [19]. If ejection was simply the result of contraction of myocardial fibres, the ejection fraction would be 15-20%, whereas the actual ejection fraction of the human heart is 60-70% [20]. This is due to the involvement of twisting. Myocardial fibres are oriented in a spherical way, so that when they contract they cause a simultaneous wringing action, resulting in an ejection fraction of 60-70%. In addition, after twisting has occurred during systole, untwisting occurs during diastole. Untwisting is known to occur mostly during the relaxation phase, suggesting that this motion assists LV relaxation, which directly influences the mechanism being studied in this work. Additionally, from a computational perspective, and although the modelling doesn't explicitly account for any torsion motions, the underlying fibre architecture that enables such motion is indirectly in the simulation, ensuring that its mechanical effects are implicitly present.

2.1.3 Anisotropy of Myocardial Tissue

The myocardial microstructure is often interpreted as mechanically anisotropic, meaning the tissue's mechanical stiffness and strength vary significantly depending on the direction of applied loads. This directional dependency is primarily attributed to the highly organized arrangement of myocytes. These myocytes are integrated into distinct muscle fibres, which in turn are often organized into laminar sheets (see Figure 2.2). This hierarchical arrangement dictates that the tissue will exhibit a differential resistance to deformation along various axes [21].

Experimental studies [22, 23] have demonstrated that the myocardium exhibits its greatest stiffness along the local myocardial fibre direction (**f**). Stiffness is progressively reduced in the sheet direction (**s**), and is lowest along the sheet-normal direction (**n**). This specific tri-directional behaviour classifies the myocardium as an orthotropic material [16], a subset of anisotropy, and constitutes a defining mechanical parameter of healthy cardiac tissue.

Therefore, such directional behaviour should be included in the model design, meaning any constitutive model for the myocardium must include direction-dependent terms, with specific invariants associated with each direction. Without accounting for anisotropy, models would fail to capture the three dimensional deformation patterns observed during the cardiac cycle, leading to inaccurate predictions and, consequently, poor performance. In this work, anisotropy is accounted for through the usage of an incompressible invariant-based constitutive law, that defines a set of invariants associated with both myofibre (**f**) and sheet (**s**) orientation, further described in the next section.

2.2 Hyperelastic Behaviour of the Passive Myocardium

Myocardial tissue has traditionally been described using hyperelastic constitutive models, as it is generally considered to be a hyperelastic material with a strong nonlinear anisotropic stress response [24]. Viscoelastic modelling approaches for myocardial tissue have gained more recent attention [25–27], although that is outside the range of this thesis. During diastole, the myocardium behaves as a soft and nearly incompressible material that undergoes large finite deformations in response to internal pressure caused by the progressive blood overload. In this scenario, the tissue response is entirely passive and dominated by the elastic properties of the underlying microstructure, particularly the orientation and interaction of myocardial fibres, sheets, and their extracellular matrix [28, 29]. To accurately represent this mechanical behaviour, the myocardium is typically modeled as a hyperelastic material, meaning that its stress response can be derived from a strain-energy function that encapsulates the tissue's intrinsic material properties. In simpler terms, this means that the stress is, by definition, the gradient of the strain-energy function.

The strain-energy function approach also facilitates the enforcement of material symmetries, such as anisotropy due to fibre orientation, through the integration of invariants associated with those directions. Moreover, it accounts for the distinction between volumetric and distortional effects, which is particularly important due to the near-incompressibility of cardiac tissue. Among several proposed models [29–33], we adopted the formulation based on the constitutive law introduced by Holzapfel and Ogden [16].

2.2.1 Strain-Energy Function

Before presenting the constitutive law used to model the myocardium behaviour during diastole, it is important to attribute a context to the kinematic invariants defined in Eqs. (A.10)–(A.13). Therefore, let us once again refer to the fibre, sheet, and sheet-normal directions, introduced in Section 2.1.2 and represented in Figure 2.2, and to the invariant I_4 associated with each of these directions.

$$I_{4f} = \mathbf{f}_0 \cdot (\mathbf{C}\mathbf{f}_0), \quad I_{4s} = \mathbf{s}_0 \cdot (\mathbf{C}\mathbf{s}_0), \quad \text{and} \quad I_{4n} = \mathbf{n}_0 \cdot (\mathbf{C}\mathbf{n}_0), \tag{2.1}$$

where

$$\sum_{i=\{f,s,n\}} I_{4i} = \mathbf{C} : (\mathbf{f}_0 \otimes \mathbf{f}_0 + \mathbf{s}_0 \otimes \mathbf{s}_0 + \mathbf{n}_0 \otimes \mathbf{n}_0) = \mathbf{C} : \mathbf{I} = I_1, \tag{2.2}$$

meaning only three of the invariants I_{4f}, I_{4s}, I_{4n} and I_1 are independent[1,2]. Additionally, according to definition (A.13), we can write

$$I_{8fs} = I_{8sf} = \mathbf{f}_0 \cdot (\mathbf{C}\mathbf{s}_0), \quad I_{8fn} = I_{8nf} = \mathbf{f}_0 \cdot (\mathbf{C}\mathbf{n}_0) \quad \text{and} \quad I_{8sn} = I_{8ns} = \mathbf{s}_0 \cdot (\mathbf{C}\mathbf{n}_0). \tag{2.3}$$

---

[1]The Frobenius product between tensors $\mathbf{A}, \mathbf{B} \in \mathbb{R}^{d \times d}$ is defined as $\mathbf{A} : \mathbf{B} = \sum_i \sum_j A_{ij} B_{ij}$.

[2]The dyadic product of vectors $\mathbf{a}, \mathbf{b} \in \mathbb{R}^d$ produces a tensor $\mathbf{A} \in \mathbb{R}^{d \times d}$ with components $A_{ij} = [\mathbf{a} \otimes \mathbf{b}]_{ij} = a_j b_i$.

Therefore, in this work, the passive myocardium is considered as an incompressible, anisotropic and hyperelastic material, fully described by the constitutive law formulated by Holzapfel and Ogden, the so called H-O model, given by:

$$
\begin{aligned}
\Psi = {} & \frac{a}{2b}\exp[b(I_1 - 3)] - 1 \\
& + \sum_{i \in \{f,s\}} \frac{a_1}{2b_i}\exp[b_i(I_{4i} - 1)^2] - 1 \\
& + \frac{a_{fs}}{2b_{fs}}\exp(b_{fs}I_{8fs}^2 - 1),
\end{aligned}
\tag{2.4}
$$

in which $\mathbf{q} = (a, b, a_f, b_f, a_s, b_s, a_{fs}, b_{fs})$ are eight positive unknown material parameters and I_1, I_{4i} and I_{8fs} are the invariants associated with each direction of the local coordinate system $\mathbf{f}$–$\mathbf{s}$–$\mathbf{n}$.

In theory, the myocardium behaves as a near-incompressible material, meaning it does not shrink or expand significantly in volume during passive filling. This behaviour is mathematically expressed as $\det \mathbf{F} = J \approx 1$. This means that, in practice, we still need to allow for small volume changes, which are penalized in the strain energy function Ψ rather than strictly enforcing $J = 1$. To achieve this, we make use of the decomposition introduced in (A.14), where the deformation gradient $\mathbf{F}$ is split into a volumetric part and an isochoric (distortional) part. As a result, we define the modified right Cauchy–Green tensor (see eq. (A.15)) to isolate the distortional component of deformation. This allows us not only to work under the practical assumption that the myocardium is, in fact, incompressible, but also to construct new invariants based on $\bar{\mathbf{C}}$ that depend only on changes in shape, and not on changes in volume. Therefore, the modified strain invariants (shown below with over bar) are now defined using $\bar{\mathbf{C}}$ instead of $\mathbf{C}$. Thus, the strain energy function in (2.4) can be rewritten in terms of modified strain invariants in the form

$$
\begin{aligned}
\Psi = {} & \frac{a}{2b}\left(\exp[b(\bar{I}_1 - 3)] - 1\right) \\
& + \sum_{i \in \{f,s\}} \frac{a_i}{2b_i}\left(\exp[b_i(\bar{I}_{4i} - 1)^2] - 1\right) \\
& + \frac{a_{fs}}{2b_{fs}}\left(\exp[b_{fs}\bar{I}_{8fs}^2] - 1\right) \\
& + \frac{1}{2}K(J - 1)^2
\end{aligned}
\tag{2.5}
$$

where the term $\frac{1}{2}K(J - 1)^2$ accounts for the incompressibility of the material, and K is a constant bulk modulus (10^6 Pa). The second Piola-Kirchhoff stress tensor ($\mathbf{S}$) can be

7

derived from (2.5) as

$$
\begin{aligned}
\mathbf{S} = 2\frac{\partial \Psi}{\partial \mathbf{C}} = {} & K(J-1)J\mathbf{C}^{-1} \\
& + a \exp[b(\bar{I}_1 - 3)]\left(J^{-\frac{2}{3}}\mathbf{I} - \frac{1}{3}\bar{I}_1\mathbf{C}^{-1}\right) \\
& + 2a_{\mathrm{f}}(\bar{I}_{4\mathrm{f}} - 1)\exp[b_{\mathrm{f}}(\bar{I}_{4\mathrm{fs}} - 1)^2]\left(\bar{\mathbf{f}}_0 \otimes \bar{\mathbf{f}}_0 - \frac{1}{3}\bar{I}_{4\mathrm{f}}\mathbf{C}^{-1}\right) \\
& + 2a_{\mathrm{s}}(\bar{I}_{4\mathrm{s}} - 1)\exp[b_{\mathrm{s}}(\bar{I}_{4\mathrm{s}} - 1)^2]\left(\bar{\mathbf{s}}_0 \otimes \bar{\mathbf{s}}_0 - \frac{1}{3}\bar{I}_{4\mathrm{s}}\mathbf{C}^{-1}\right) \\
& + a_{\mathrm{fs}}\bar{I}_{8\mathrm{fs}}\exp[b_{\mathrm{fs}}\bar{I}_{8\mathrm{fs}}^2]\left(\bar{\mathbf{s}}_0 \otimes \bar{\mathbf{f}}_0 + \bar{\mathbf{f}}_0 \otimes \bar{\mathbf{s}}_0 - \frac{1}{3}\bar{I}_{8\mathrm{fs}}\mathbf{C}^{-1}\right),
\end{aligned}
\tag{2.6}
$$

and the Cauchy stress tensor defined as

$$
\sigma = \frac{1}{J}\mathbf{F}\mathbf{S}\mathbf{F}^T.
\tag{2.7}
$$

2.2.2 Simulation of LV Passive Diastolic Filling

The LV diastolic filling process is described by a quasi-static pressure-loaded boundary value problem over the computational domain Ω occupied by the LV geometry. The equilibrium equation at the current configuration $\Omega(t)$ is given by:

$$
\begin{cases}
\nabla \cdot \sigma + \mathbf{b} = 0 & \text{in } \Omega(t), \\
\sigma \cdot \mathbf{n} = \mathbf{t} & \text{on } \Gamma^N, \\
\mathbf{u} = \mathbf{u}_0 & \text{on } \Gamma^D.
\end{cases}
\tag{2.8}
$$

Here, $\mathbf{b}$ is the body force density per unit volume, $\mathbf{n}$ is the normal direction of $\partial\Omega$, $\mathbf{t}$ is the traction force, Γ^N and Γ^D are the Neumann and Dirichlet boundaries. This problem is solved using the finite-element approach implemented in a general-purpose finite-elements package ABAQUS[3], which is used to simulate the biomechanical LV models during diastolic filling. The model incorporates a high-resolution mesh derived from previous studies, comprising 53,548 nodes and 48,050 hexahedral elements, ensuring an anatomically realistic geometry and suited to serve as a foundation for the simulations described in this chapter. Physiologically motivated boundary conditions were applied to replicate in vivo cardiac constraints: the basal surface of the LV was fixed along both the long-axis (W_l-axis) and the circumferential direction (W_c-axis), while permitting radial expansion to mimic natural deformation, as can be seen in Fig. 2.3. A pressure load, linearly ramped from 0 to 8 mmHg over 25 equally spaced increments was applied to the endocardial surface, and the resulting mechanical fields were recorded at each step. This quasi-static pressure-loading protocol emulates the early filling phase of the cardiac cycle.

---

[3]Simulia, Providence, RI, USA
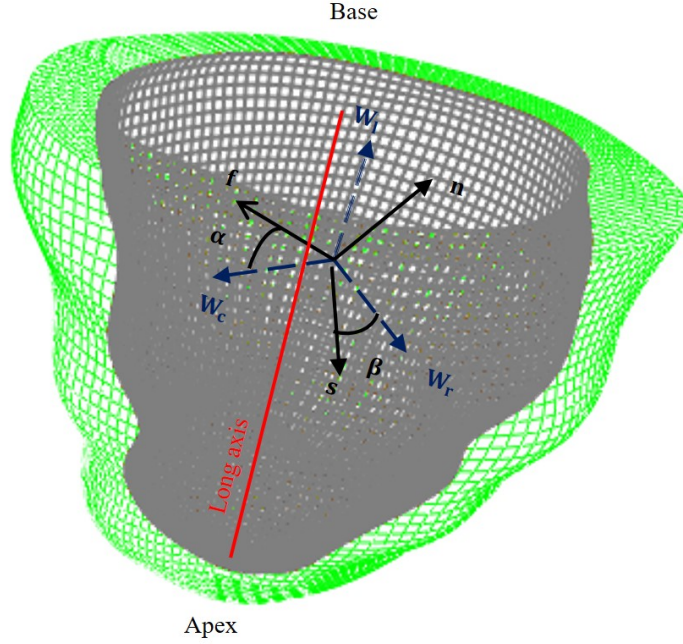
Figure 2.3: Visualization of the LV geometry. (**f**, **s**, **n**) represent the coordinate system, and (**W**$_c$, **W**$_l$, **W**$_r$) are coordinate axes that indicate the local circumferential, longitudinal and radial axes. The helix angle α is defined to be the angle between **f** and **W**$_c$ in the plane spanned by **W**$_c$ and **W**$_l$, and the sheet angle β is defined to be the angle between **s** and **W**$_r$ in the plane spanned by **W**$_l$ and **W**$_r$. The grey colour represents the epicardium and the green colour represents the endocardium. Adapted from [34].

Gao et al. [35] showed that the eight parameters in (2.4) are strongly correlated, which makes it difficult to uniquely identify them from limited and noisy in vivo measurements. Still, their results indicate that the stress–strain behaviour along the fibre direction can be reliably estimated, even with sparse data. Along similar lines, Hadjicharalambous et al. [36] proposed a reduced version of the H-O model with only one fitting parameter, aiming to balance model fidelity with parameter identifiability in clinical applications. Following [35], we can group original eight parameters of (2.4) into four, such that

$$
\begin{cases}
a = q_1 a_0 & b = q_1 b_0 \\
a_\mathrm{f} = q_2 a_{f0} & a_\mathrm{s} = q_2 a_{s0} \\
b_\mathrm{f} = q_3 b_{f0} & b_\mathrm{s} = q_3 b_{s0} \\
a_\mathrm{fs} = q_4 a_{fs0} & b_\mathrm{fs} = q_4 b_{fs0},
\end{cases}
\tag{2.9}
$$

where $\mathbf{q} = (q_1, \cdots, q_4) \in [0.1, 5]^4$ are now the four parameters to be inferred from in vivo data, while $a_0, b_0, a_{f0}, a_{s0}, b_{f0}, b_{s0}, a_{fs0}, b_{fs0}$ are reference values from the published literature [37][4]. This procedure is further described in Section 4.3.

---

[4]The reference values are, up to 2 decimal places: $a_0 = 0.22$, $b_0 = 1.62$, $a_{f0} = 2.43$, $a_{s0} = 0.56$, $b_{f0} = 1.83$, $b_{s0} = 0.77$, $a_{fs0} = 0.39$, and $b_{fs0} = 1.70$.

STATISTICAL EMULATION

This thesis focuses on emulating the behaviour of the LV during passive diastolic filling by replicating the results obtained from solving the system of PDEs in (2.9). This chapter outlines the methodology used to that end. First, we justify the need for emulation and define what it means to emulate a physiological system, distinguishing between a simulator and an emulator. We then discuss the design of computer experiments as a means of approximating continuous functions using a finite set of data points. Finally, we introduce the chosen emulation method and illustrate its use through two hypothetical examples.

3.1 Definition

As explained in Chapter 2, the heart, particularly the LV, can be characterized as a hyperelastic, nearly incompressible material with an anisotropic response to applied forces. This mechanical behavior can be captured by a set of PDEs which, when complemented with appropriate boundary conditions, fully describe the deformation of the LV throughout the diastolic filling phase. By solving this boundary value problem using a selected numerical method, one can accurately predict the mechanical response of the LV from the onset of diastole to its conclusion.

In theory, this physics-based simulation approach represents the ideal case scenario for accurately capturing the LV biomechanical behavior. However, in practice, solving these models is computationally expensive, which often require several days of runtime, particularly when solving many instances for model personalization. Such computational costs make these models impractical in real-world scenarios, especially in a clinical setting where near-instantaneous results are essential.

To address this limitation, statistical emulation offers a suitable alternative. Instead of solving the governing PDEs repeatedly for the defined number of samples, an emulator approximates the simulator's input–output mapping based on a finite number of computationally chosen simulation results. Once trained, the emulator can produce near-instantaneous predictions for a fraction of the computational cost.

In this thesis, the mechanistic model of interest is expressed in the form of a computational simulator. Given a set of input parameters $\boldsymbol{\theta}$ and additional model (boundary) conditions $\mathbf{z}$, the simulator ζ returns an output $\mathbf{m}(\boldsymbol{\theta})$ that characterises the system response:

$$\mathbf{m}(\boldsymbol{\theta}) = \zeta(\boldsymbol{\theta}, \mathbf{z}). \tag{3.1}$$

In the context of this work, the system corresponds to the behaviour of the LV during passive diastolic filling. However, evaluating $\zeta(\cdot)$ can become computationally infeasible, particularly when the simulator involves solving nonlinear PDEs, as in our case (see Eq. (2.8)). This cost limits the use of the simulator in the majority of tasks in a clinical setting, where fast results are a priority.

In contrast, data-driven modelling offers an alternative approach. Rather than encoding physical laws, it learns patterns directly from data. While generally faster to evaluate, such models lack interpretability and theoretical foundation. However, the strengths of both approaches can be combined through a process known as statistical emulation [38–41].

In emulation, we construct a statistical surrogate model, the so-called *emulator*, that mimics the input–output behaviour of the simulator. The emulator is trained on a finite set of simulation results generated by carefully sampling the input space. Formally, the emulator is a function η that approximates ζ:

$$\hat{\mathbf{m}}(\boldsymbol{\theta}) = \eta(\boldsymbol{\theta}), \tag{3.2}$$

where η is a regression model fitted to pairs $\{\boldsymbol{\theta}^{(i)}, \zeta(\boldsymbol{\theta}^{(i)})\}$ for $i = 1, \ldots, N$. Unlike the simulator, η is inexpensive to evaluate and can produce rapid predictions, making it suitable for the considered tasks. It is also important to note that, while η does not explicitly model the physical mechanisms governing a specific system, which, at first, may seem like a significant flaw, it inherits the simulator's behaviour through the training data [41], therefore making them a reliable method to replicate physical behaviour.
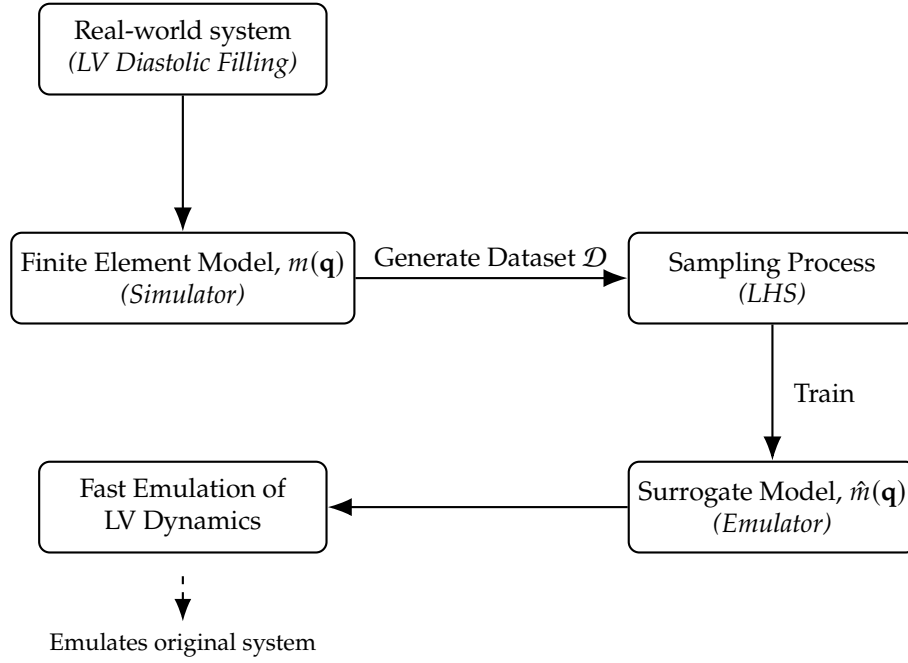
Figure 3.1: The idea behind surrogate modelling: the real-world cardiac system can be described and consequently simulated with a forward finite element model. This model generates data that is used to train a surrogate model, which learns the underlying mechanisms of LV dynamics and becomes able to replicate those mechanisms efficiently, instead of running the simulator, $m(\mathbf{q})$, each time new data is presented. Based on [34].

The training simulations should be obtained by exploiting the fact that all N runs used to fit the surface can be done in parallel, even before seeing any experimental data. Whenever a simulation from the underlying mathematical model is needed at a point that has not been visited before, the costly value $\mathbf{m}(\mathbf{q})$ is replaced by a fast prediction from the surrogate model $\hat{\mathbf{m}}(\boldsymbol{\theta})$.

3.2 Non-Parametric Bayesian Regression

In classical parametric models, the model structure is defined a priori and assumes a fixed number of parameters, regardless of the size or complexity of the data. While this approach is often computationally efficient, it lacks the ability to capture nonlinear input–output relationships, particularly when the underlying physical system is prone to variability.

To illustrate the limitations of parametric models, we first consider a classical linear regression setup. Let $\mathcal{X} \subseteq \mathbb{R}^d$ denote the input space and $\mathcal{Y} \subseteq \mathbb{R}$ the output space. We consider the general regression problem of learning an unknown function $f : \mathcal{X} \to \mathcal{Y}$ from noisy observations $\mathcal{D} = \{(\mathbf{x}_i, y_i)\}_{i=1}^n$ and fixed weights $\mathbf{w} \in \mathbb{R}^d$, where

$$y_i = f(\mathbf{x}_i) + \varepsilon_i, \qquad f(\mathbf{x}_i) = \mathbf{x}_i^T \mathbf{w} \tag{3.3}$$

and ε_i represents additive noise, which we further assume to follow an independent, identically distributed Gaussian distribution with zero mean and variance σ_n^2:

$$\varepsilon_i \sim \mathcal{N}(0, \sigma^2) \tag{3.4}$$

This assumption yields the likelihood:

$$
\begin{aligned}
p(\mathbf{y} \mid \mathbf{X}, \mathbf{w}) &= \prod_{i=1}^{n} p(y_i \mid \mathbf{x}_i, \mathbf{w}) \\
&= \prod_{i=1}^{n} \frac{1}{\sqrt{2\pi}\sigma} \exp\left(-\frac{(y_i - \mathbf{x}_i^T \mathbf{w})^2}{2\sigma^2}\right) \\
&= \frac{1}{(2\pi\sigma^2)^{n/2}} \exp\left(-\frac{1}{2\sigma^2}\|\mathbf{y} - \mathbf{X}^T\mathbf{w}\|^2\right) \\
&= \mathcal{N}(\mathbf{y} \mid \mathbf{X}^T\mathbf{w}, \sigma^2\mathbf{I})
\end{aligned}
\tag{3.5}
$$

where $\|\cdot\|$ denotes the Euclidean norm. A Bayesian (parametric) formulation involves specifying a prior distribution over the parameters, expressing our beliefs about the parameters before we look at the observations. Therefore, we put a zero mean Gaussian prior with covariance matrix Σ_p on the weights:

$$\mathbf{w} \sim \mathcal{N}(\mathbf{0}, \mathbf{\Sigma}_p) \tag{3.6}$$

and the posterior is obtained using Bayes' rule:

$$\text{posterior} = \frac{\text{likelihood} \times \text{prior}}{\text{marginal likelihood}}, \qquad p(\mathbf{w} \mid \mathbf{y}, \mathbf{X}) = \frac{p(\mathbf{y} \mid \mathbf{X}, \mathbf{w})\pi(\mathbf{w})}{p(\mathbf{y} \mid \mathbf{X})}. \tag{3.7}$$

However, constraining the model specification in such way is not appropriate for the type of surrogate modelling required in this work. The forward simulator exhibits a complex and nonlinear response governed by PDEs. Attempting to capture this behavior with a fixed, finite set of basis functions would likely result in either underfitting, if the model is too simple, or overfitting, if made arbitrarily complex. Moreover, the parameter inference problem derived from such models would not appropriately quantify uncertainty, which is essential for ill-posed inverse problems. To bypass this limitation, we explore a non-parametric approach.

A non-parametric Bayesian model is built upon a Bayesian framework based on an infinite-dimensional parameter space. The parameter space is typically chosen as the set of all possible solutions for a given learning problem. In this framework, we define a prior distribution Π over an infinite-dimensional space of functions $\mathcal{F}$ and condition it on observed data to obtain a posterior distribution. This essentially means that we allow for the model to grow its complexity according to the data that is progressively being presented.

The regression model introduced in Eq. (3.3) then becomes:

$$y_i = f(\mathbf{x}_i) + \varepsilon_i, \quad f \in \mathcal{F} \tag{3.8}$$

The non-parametric Bayesian approach proceeds by placing a prior distribution Π over the function space $\mathcal{F}$, such that $f \sim \Pi$, and subsequently computing the posterior distribution $\Pi(\cdot \mid \mathcal{D})$ using Bayes' theorem, similarly to (3.7). Formally, the posterior distribution over functions is given by:

$$\Pi(f \mid \mathcal{D}) = \frac{p(\mathbf{y} \mid f, \mathbf{X})\,\Pi(f)}{p(\mathbf{y} \mid \mathbf{X})}, \tag{3.9}$$

where $p(\mathbf{y} \mid f, \mathbf{X})$ is the likelihood and $\Pi(f)$ is the prior over functions.

The precision of this approach strongly depends on the definition of the prior, i.e, the covariance function, which encapsulates the beliefs about the function f before seeing any data. A poor choice of this prior will force the posterior to reflect poor assumptions about the problem, regardless of how good the data is.

3.2.1 Gaussian Processes

A GP constitutes a stochastic process $\{f(\mathbf{x})\}_{\mathbf{x} \in \mathcal{X}}$ such that any finite collection of function values $\{f(\mathbf{x}_1), f(\mathbf{x}_2), \ldots, f(\mathbf{x}_k)\}$ follows a multivariate Gaussian distribution. This definition implies that a GP is completely specified by a mean function $m : \mathcal{X} \to \mathbb{R}$ and a covariance function $k : \mathcal{X} \times \mathcal{X} \to \mathbb{R}$, defined as:

$$
\begin{aligned}
m(\mathbf{x}) &= \mathbb{E}[f(\mathbf{x})], \\
k(\mathbf{x}, \mathbf{x}') &= \mathbb{E}[(f(\mathbf{x}) - m(\mathbf{x}))(f(\mathbf{x}') - m(\mathbf{x}'))].
\end{aligned}
\tag{3.10}
$$

The process is denoted by:

$$f \sim \mathcal{GP}(m(\mathbf{x}), k(\mathbf{x}, \mathbf{x}')). \tag{3.11}$$

Given a finite set of inputs $\mathbf{X} = \{\mathbf{x}_1, \mathbf{x}_2, \ldots, \mathbf{x}_n\}$, the vector of corresponding function values $\mathbf{f} = [f(\mathbf{x}_1), \ldots, f(\mathbf{x}_n)]^T$ follows:

$$\mathbf{f} \sim \mathcal{N}(\boldsymbol{\mu}, \mathbf{K}), \tag{3.12}$$

where $\boldsymbol{\mu} = [m(\mathbf{x}_1), \ldots, m(\mathbf{x}_n)]^T$ and $\mathbf{K}$ is the covariance matrix with entries $K_{ij} = k(\mathbf{x}_i, \mathbf{x}_j)$. More explicitly, the prior distribution of the joint vector

$$
\begin{bmatrix}
f(x) \\
f(x_1) \\
\vdots \\
f(x_n)
\end{bmatrix}
$$

is given by:

$$\mathcal{N}\left(\mu, \begin{bmatrix} k(x,x) & k(x,x_1) & \dots & k(x,x_n) \\ k(x_1,x) & k(x_1,x_1) & \dots & k(x_1,x_n) \\ \vdots & \vdots & \ddots & \vdots \\ k(x_n,x) & k(x_n,x_1) & \dots & k(x_n,x_n) \end{bmatrix}\right), \tag{3.13}$$

which fully specifies the GP prior.

Now consider the regression setting with noisy observations $\mathcal{D} = \{(\mathbf{x}_i, y_i)\}_{i=1}^n$ modeled by the likelihood:

$$y_i \mid f(\mathbf{x}_i) \sim \mathcal{N}(f(\mathbf{x}_i), \sigma^2). \tag{3.14}$$

Combining this likelihood with the GP prior $f \sim \mathcal{GP}(m(\mathbf{x}), k(\mathbf{x}, \mathbf{x}'))$, the joint distribution of the observed outputs $\mathbf{y} = [y_1, \dots, y_n]^T$ and the function values at test inputs $\mathbf{X}_* = \{\mathbf{x}_1^*, \dots, \mathbf{x}_{n_*}^*\}$ is:

$$\begin{bmatrix} \mathbf{y} \\ \mathbf{f}_* \end{bmatrix} \sim \mathcal{N}\left(\begin{bmatrix} \mu \\ \mu_* \end{bmatrix}, \begin{bmatrix} \mathbf{K} + \sigma^2\mathbf{I} & \mathbf{K}_* \\ \mathbf{K}_*^T & \mathbf{K}_{**} \end{bmatrix}\right), \tag{3.15}$$

where the submatrices are defined as

$$\mathbf{K} = k(\mathbf{X}, \mathbf{X}) \in \mathbb{R}^{n \times n} \text{ such that } (K(\mathbf{X}, \mathbf{X}))_{ij} = k(x^{(i)}, x^{(j)}),$$

$$\mathbf{K}_* = k(\mathbf{X}, \mathbf{X}_*) \in \mathbb{R}^{n \times n_*} \text{ such that } (K(\mathbf{X}, \mathbf{X}_*))_{ij} = k(x^{(i)}, x_*^{(j)}), \tag{3.16}$$

$$\mathbf{K}_{**} = k(\mathbf{X}_*, \mathbf{X}_*) \in \mathbb{R}^{n_* \times n_*} \text{ such that } (K(\mathbf{X}_*, \mathbf{X}_*))_{ij} = k(x_*^{(i)}, x_*^{(j)}).$$

From the derivation of the joint distribution in (3.15), we obtain the posterior predictive distribution over test points $\mathbf{X}_*$ by standard Gaussian conditioning. The result is as follows.

$$\mathbf{f}_* \mid \mathbf{y}, \mathbf{X}, \mathbf{X}_* \sim \mathcal{N}(\mu_{*|y}, \Sigma_{*|y}), \tag{3.17}$$

where

$$\mu_{*|y} = \mu_* + \mathbf{K}_*^T(\mathbf{K} + \sigma^2\mathbf{I})^{-1}(\mathbf{y} - \mu),$$

$$\Sigma_{*|y} = \mathbf{K}_{**} - \mathbf{K}_*^T(\mathbf{K} + \sigma^2\mathbf{I})^{-1}\mathbf{K}_*. \tag{3.18}$$

Usually, for computational simplicity, a zero mean prior is assumed, i.e., $\mu = 0$, which yields:

$$\mu_{*|y} = \mathbf{K}_*^T(\mathbf{K} + \sigma^2\mathbf{I})^{-1}\mathbf{y},$$

$$\Sigma_{*|y} = \mathbf{K}_{**} - \mathbf{K}_*^T(\mathbf{K} + \sigma^2\mathbf{I})^{-1}\mathbf{K}_*. \tag{3.19}$$

In this expression, the variance function $\Sigma_{*|y}$ reveals that the uncertainty in predictions depends solely on the input values $\mathbf{X}$ and $\mathbf{X}_*$, not on the observed outputs $\mathbf{y}$, which constitutes a characteristic property of Gaussian distributions [42].

3.2.2 Covariance Functions

Although both a mean and a covariance function are required to fully define GP, it is typically the covariance function that requires greater considerations. Usually, the mean is either assumed to be zero or can be centered out by preprocessing the data. If the data exhibits a known parametric mean structure, one can subtract it prior to GP modelling, yielding residuals centered around zero[1]. This is the approach adopted in this thesis, where we assume a zero mean process and focus entirely on modelling the correlations and smoothness structure encoded in the covariance function.

For any two inputs $\mathbf{x}, \mathbf{x}' \in \mathcal{X}$, the covariance function $k(\mathbf{x}, \mathbf{x}')$ quantifies the degree of similarity or correlation between the function values $f(\mathbf{x})$ and $f(\mathbf{x}')$. The stronger the correlation, the more tightly $f(\mathbf{x})$ and $f(\mathbf{x}')$ are coupled in the posterior inference. However, not every function qualifies as a valid covariance function. In order to define a proper GP, the kernel function must satisfy the condition of positive and semi-definite. This means that for any finite set of inputs $\{\mathbf{x}_1, \ldots, \mathbf{x}_n\}$, the resulting covariance matrix $\mathbf{K} \in \mathbb{R}^{n \times n}$, with entries $K_{ij} = k(\mathbf{x}_i, \mathbf{x}_j)$, must satisfy

$$k(\mathbf{x}, \mathbf{x}') = k(\mathbf{x}', \mathbf{x}) \quad \forall \mathbf{x}, \mathbf{x}' \in \mathcal{X}$$

$$\sum_{i=1}^{n} \sum_{j=1}^{n} c_i c_j k(\mathbf{x}_i, \mathbf{x}_j) \geq 0 \quad \forall n \in \mathbb{N}, \mathbf{x}_1, \ldots, \mathbf{x}_n \in \mathcal{X}, c_1, \ldots, c_n \in \mathbb{R}. \tag{3.20}$$

This is equivalent to requiring that all covariance matrices formed by evaluating k at finite sets of points are positive semi-definite. Among the various families of covariance functions, this work focuses on the Matérn family, due to its greater ability to capture the relations presented by our data. For more information on different classes of kernels, see [42].

The Matérn class is a class of kernels that generalizes the smoothness properties of the GP prior through a continuous parameter $\nu > 0$. It is defined as:

$$k_{\text{Matérn}}(r) = \sigma_f^2 \cdot \frac{2^{1-\nu}}{\Gamma(\nu)} \left(\frac{\sqrt{2\nu}r}{\ell} \right)^{\nu} K_{\nu} \left(\frac{\sqrt{2\nu}r}{\ell} \right), \tag{3.21}$$

with $r = \|\mathbf{x} - \mathbf{x}'\|$ and positive parameters ν and ℓ. K_{ν} is a modified Bessel function of the second kind, $\Gamma(\cdot)$ is the Gamma function. The hyperparameters σ_f, signal variance, and ℓ, characteristic lengthscale, control the vertical and horizontal scales, respectively. This covariance function has a spectral density

$$S(s) = \frac{2^D \pi^{\frac{D}{2}} \Gamma(\nu + \frac{D}{2})(2\nu)^{\nu}}{\Gamma(\nu)\ell^{2\nu}} \left(\frac{2\nu}{\ell^2} + 4\pi^2 s^2 \right)^{-\left(\nu + \frac{D}{2}\right)} \tag{3.22}$$

in D dimensions. This kernel defines a stationary, isotropic covariance structure with controlled smoothness, as the kernel depends only on the norm of the difference between

---

[1]It is also possible to define a parametric mean function and infer its parameters jointly with the GP. In this case, the GP can be viewed as operating on the residual structure after accounting for the parametric trend. See Rasmussen and Williams (2006), Chapter 2.

input points. As ν increases, the resulting sample paths become progressively smoother. Importantly, when $\nu = p + \frac{1}{2}$ for integer $p \geq 0$, the kernel simplifies to a closed-form expression involving exponentials and polynomials, removing the need to evaluate Bessel functions [42]. If $\nu = 1/2$, then the path is once continuous and nowhere differentiable. This special case is also referred to as the Ornstein–Uhlenbeck process. If $\nu \to \infty$, then the process $f(\mathbf{x})$ becomes infinitely differentiable. Both these extremes are usually less useful in our context. For $\nu = 1/2$, the process becomes very rough, and for $\nu \to \infty$, it is often unrealistic to assume infinite smoothness when working with finite noisy training data and no strong prior belief about the regularity of the underlying simulator.

The values $\nu = 3/2$ and $\nu = 5/2$ are the most commonly used. For $\nu = 3/2$, the kernel becomes

$$k_{\nu=3/2}(r) = \sigma_f^2 \left(1 + \frac{\sqrt{3}r}{\ell}\right) \exp\left(-\frac{\sqrt{3}r}{\ell}\right), \tag{3.23}$$

resulting in functions that are once mean-squared (MS) differentiable. For $\nu = 5/2$, which is the kernel adopted in this thesis, we have

$$k_{\nu=5/2}(r) = \sigma_f^2 \left(1 + \frac{\sqrt{5}r}{\ell} + \frac{5r^2}{3\ell^2}\right) \exp\left(-\frac{\sqrt{5}r}{\ell}\right), \tag{3.24}$$

and the resulting process is twice MS differentiable.

Additionally, it is also important to clarify that the notion of differentiability used here refers to MS differentiability, rather than classical pointwise differentiability. Specifically, a stochastic process $f(\mathbf{x})$ is said to be k-times MS differentiable if the k-th derivative $\frac{d^k f}{dx^k}$ exists in the sense of L^2 convergence, i.e.,

$$\mathbb{E}\left[\left(\frac{d^k f(\mathbf{x})}{dx^k}\right)^2\right] < \infty. \tag{3.25}$$

In the context of the Matérn class, the process f is k-times MS differentiable if and only if $\nu > k$. Thus, the Matérn 5/2 kernel guarantees that the GP prior generates functions that are twice differentiable in the MS sense.

This property is particularly relevant for the application considered in this thesis. The displacement fields and stress responses in such systems are typically smooth and at least once differentiable with respect to spatial coordinates. Choosing a kernel that generates twice-differentiable priors allows the emulator to capture the gradients in the input–output relationships without forcing unrealistic levels of smoothness, as would be the case with $\nu \to \infty$.
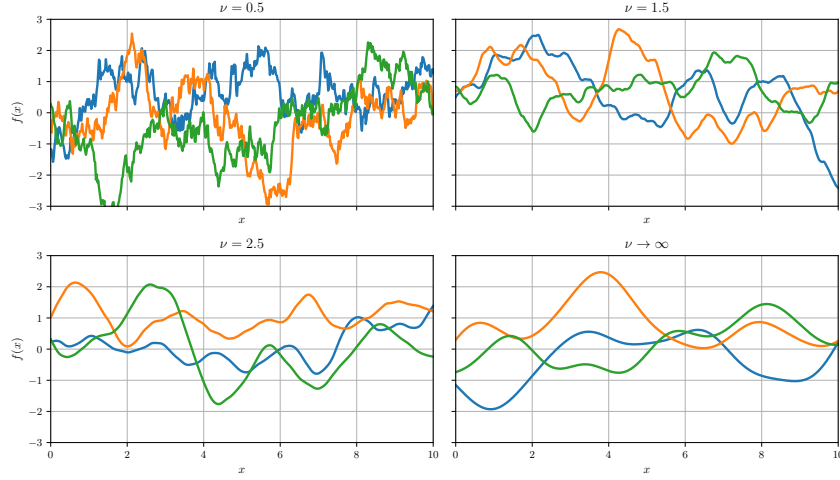
Figure 3.2: Random functions drawn from GPs with Matérn covariance functions for different values of ν, using fixed hyperparameters $\ell = 1$ and $\sigma_f^2 = 1$. Samples were generated by evaluating the prior over 500 equally spaced input points.

3.2.3 Hyperparameter Optimization

The Matérn 5/2 kernel used in this work introduces a set of hyperparameters $\boldsymbol{\theta} = \{\ell, \sigma_f^2\}$, corresponding to the characteristic lengthscale and signal variance, respectively. Observation noise variance, σ^2, is also inherently present in the model specification.

While direct inference of hyperparameters is not possible, we can adopt a Bayesian approach to find the optimal values by maximizing the marginal likelihood. The marginal likelihood is obtained by integrating over the latent function values $\mathbf{f}$:

$$p(\mathbf{y} \mid \mathbf{X}, \boldsymbol{\theta}) = \int p(\mathbf{y} \mid \mathbf{f}, \sigma^2) \, p(\mathbf{f} \mid \mathbf{X}, \ell, \sigma_f^2) \, d\mathbf{f}. \tag{3.26}$$

Due to the conjugacy of the Gaussian likelihood and the GP prior, this integral has a closed-form expression:

$$\log p(\mathbf{y} \mid \mathbf{X}, \boldsymbol{\theta}) = -\frac{1}{2}\mathbf{y}^T \mathbf{K}_y^{-1} \mathbf{y} - \frac{1}{2}\log |\mathbf{K}_y| - \frac{n}{2}\log(2\pi), \tag{3.27}$$

where $\mathbf{K}_y = \mathbf{K}(\mathbf{X}, \mathbf{X}; \ell, \sigma_f^2) + \sigma^2 \mathbf{I}$ is the marginal covariance matrix evaluated using the Matérn 5/2 kernel. The optimal hyperparameters are found by solving:

$$\boldsymbol{\theta}^* = \underset{\boldsymbol{\theta}}{\operatorname{argmax}} \log p(\mathbf{y} \mid \mathbf{X}, \boldsymbol{\theta}). \tag{3.28}$$

This optimization is typically performed using gradient-based methods, as the gradients of the log marginal likelihood with respect to each hyperparameter θ_j can be computed analytically as:

$$\frac{\partial}{\partial \theta_j} \log p(\mathbf{y} \mid \mathbf{X}, \boldsymbol{\theta}) = \frac{1}{2}\operatorname{trace}\left[\left(\boldsymbol{\alpha}\boldsymbol{\alpha}^T - \mathbf{K}_y^{-1}\right)\frac{\partial \mathbf{K}_y}{\partial \theta_j}\right], \tag{3.29}$$

where $\boldsymbol{\alpha} = \mathbf{K}_y^{-1}\mathbf{y}$.

3.3 Experiments

This chapter presents two illustrative examples to demonstrate the functioning of a GPR. First, we fit a GP to a sinusoidal function to try and approximate the non-linear behaviour. In the second example, we extend the principles in the first example to a more applied setting. Specifically, we use a GP to emulate the behaviour of a simple cardiac simulator. With these example, we show that it is possible to replicate the results from the simulator within a fraction of time while maintaining the accuracy of the results.

3.3.1 Sinusoidal Function

In this example, we use a GP to approximate the behaviour of a highly non-linear trigonometric function, defined as

$$f(x) = \sqrt{x} \sin(1.5x) e^{\left(-\frac{(x-5)^2}{10}\right)} + 0.1x, \tag{3.30}$$

which exhibits multiple inflection points and irregular patterns, often found in real-case physical systems.

We first show prior samples from a GP with a Matérn 5/2 kernel. Since the model has not yet seen any observations, all functions drawn from the prior are equally likely under the model assumptions. As established in (3.6), we assume a zero mean Gaussian prior distribution. Figure 3.3 shows ten possible functions sampled from the prior distribution. The only information those ten functions have about $f(x)$ is encoded through the covariance function.
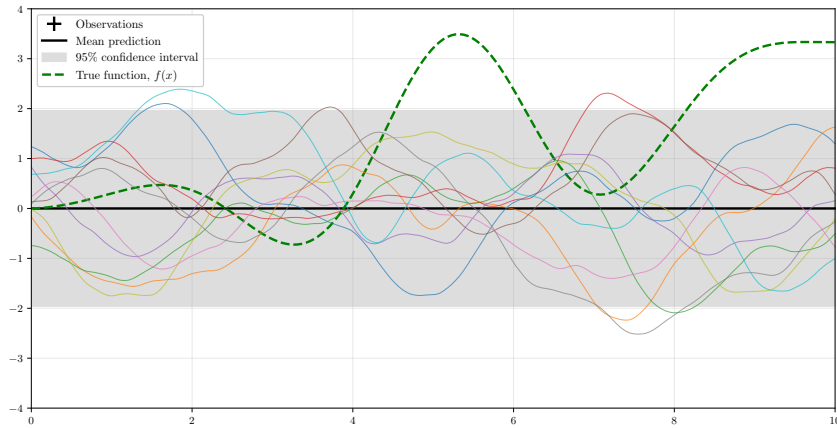
Figure 3.3: 10 samples from the prior distribution of a GP with Matérn 5/2 kernel. The model has not observed any data, so all functions consistent with the prior are equally likely.

Next, we condition the GP on n observed data points sampled non-uniformly from the input domain. The goal is to show how the model updates its predictions and associated uncertainties as more information becomes available. When the number of observations is low, the posterior distribution interpolates the few known data points but presents wide

confidence intervals in regions with no data. As n increases, the GP gains more local information and becomes more confident, reflected in narrower predictive intervals and more accurate mean estimates. Figure 3.4 illustrates this process for $n = 5, 20, 50$, and 100 observations.

(a) $n = 5$ **(b)** $n = 20$

(c) $n = 50$ **(d)** $n = 100$
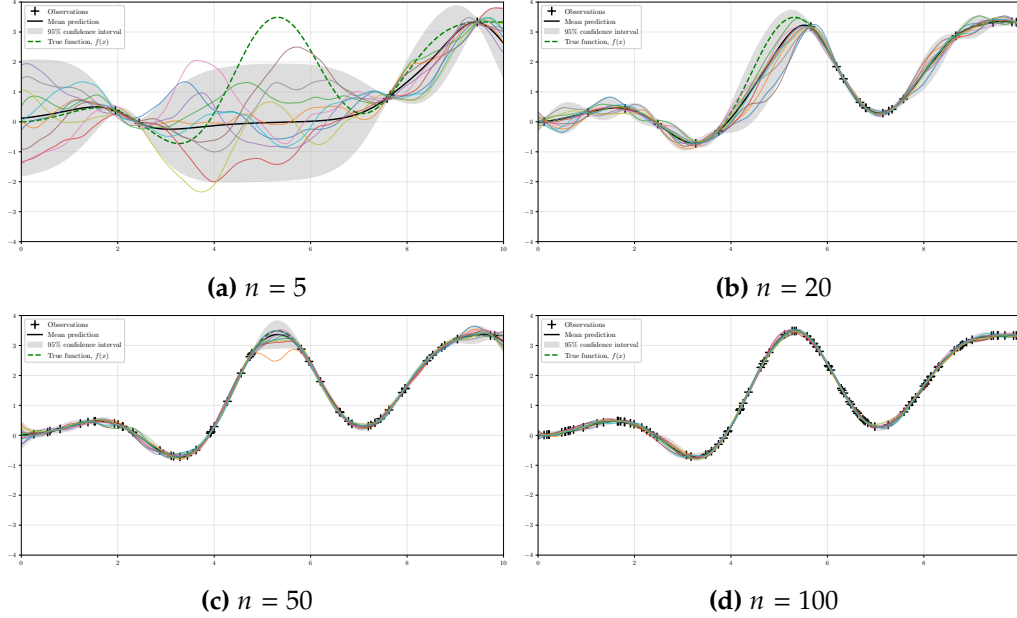
Figure 3.4: Posterior predictions from a GP with Matérn 5/2 kernel as the number of training points increases. The shaded area represents a 95% confidence interval around the posterior mean. As more data becomes available, uncertainty decreases and the GP more closely approximates the true function.

To better visualize the interpolation capability of the GP, Figure 3.5 isolates the posterior mean prediction and compares it directly to the true function.
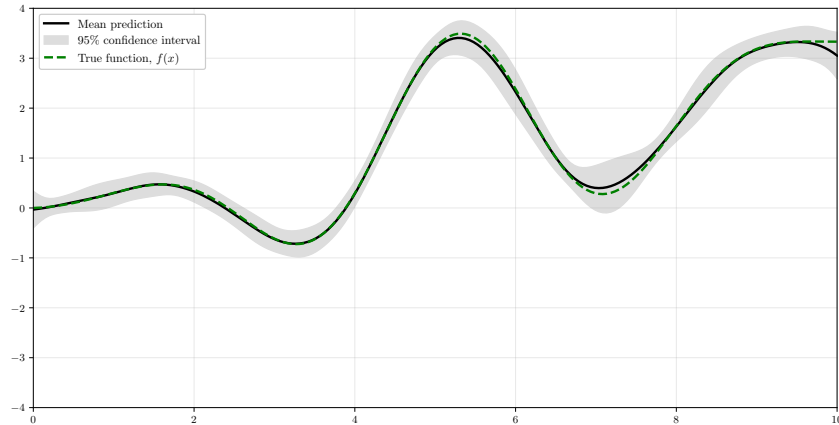
Figure 3.5: Comparison between the GP posterior mean and the true function. As can be seen, the GP naturally presents larger uncertainties in regions with fewer observations, specifically around $x = 5.5$ and $x = 7$. Nevertheless, the GP can capture the general behaviour of the function, even in regions with fewer observation points.

3.3.2 End Diastolic Volume

Following the example from the previous subsection, we now apply a GPR to a real scenario. The goal is to emulate the output of a simplified cardiac simulator, which computes the end diastolic volume (EDV) of the LV under a specific pressure load. Because we know the pressure is ramped linearly from 0 to 8 mmHg, and because the pressure–volume relation is exponential due to tissue properties [43], we can simulate the EDV under this known pressure loading. Then, we emulate the mapping from the material parameters to the resulting EDV at the final pressure.

$$\mathbf{q} \mapsto \text{EDV} \, (p = 8 \text{ mmHg}). \tag{3.31}$$

Figure 3.6 shows the comparison between true simulator outputs and the corresponding GP predictions on six test points.
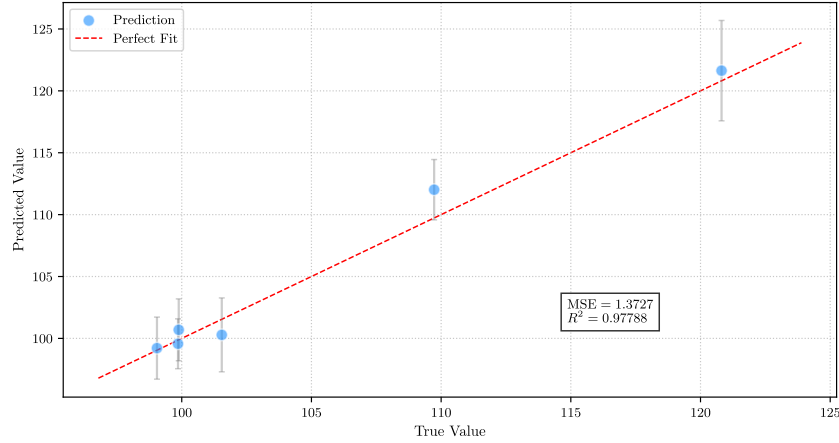
Figure 3.6: Comparison between the ground truth EDV values produced by the cardiac simulator and the GP predictions on a test set.

The idea of this setup is to show that a GP can accurately emulate a nonlinear biomechanical simulator by learning the mapping from material parameters to EDV. Once trained, the GP can produce EDV predictions in milliseconds, instead of having to run the simulator for each set of new parameters.

Surrogate Model for Passive LV Dynamics

This chapter presents the core methodological contributions of this work, focused on the development and application of a computationally efficient surrogate model for the analysis and inference of biomechanical parameters in cardiac simulations. Using synthetic data generated from multiple finite element method (FEM) simulations of LV dynamics, we train independent statistical emulators capable of approximating the outputs of high-fidelity models with minimal computational cost at a high speed rate. The effect of possible model parameter perturbations is then assessed through both global and local sensitivity analysis. Besides that, we took advantage of the built-in attribute of GPs, which is *principled prediction uncertainty:* GPs are able to quantify prediction uncertainty of the unknown function (physiological relation) we're trying to optimize. This uncertainty comes from the fact that GPs define a prior distribution on a function space that is updated iteratively through Bayesian inference [44]. By doing so, the model is able to predict a specific output as well as quantify the level of uncertainty associated with that prediction. Finally, we explore the concept of Bayesian inference by formulating the inverse problem and inferring unknown material parameters.

4.1 Surrogate Model

This section focuses on the description of the modelling process. We develop a framework to emulate the results of the forward simulations described in Section 2.2.2. This section clarifies the adopted architecture as well as the training and evaluation processes. The surrogate aims to predict the six-dimensional output vector $\mathbf{y} = (\alpha_0, \beta_0, \alpha_1, \beta_1, \alpha_2, \beta_2)$ from a four-dimensional parameter vector $\mathbf{q} = (q_1, q_2, q_3, q_4)$, with the main goal of reducing the computational burden, which may prevent more complex tasks.

4.1.1 Model Specification

When modelling a multi-dimensional output vector $\mathbf{y} \in \mathbb{R}^6$ using GPs, one can design the surrogate in two fundamental ways: either train k independent single-output GP, with k

being the number of output features; or train a multi-output GP. The distinction lies in how the dependency structure among output components is handled.

In the single-output formulation, each output dimension y_k is modeled independently as a realization of a scalar-valued GP:

$$y_k(\mathbf{q}) \sim \mathcal{GP}(m_k(\mathbf{q}), k_k(\mathbf{q}, \mathbf{q}')), \quad k = 1, \ldots, 6, \tag{4.1}$$

where $m_k(\cdot)$ is the mean function, which is usually taken as zero without loss of generality, and $k_k(\cdot, \cdot)$ is a kernel function tailored to the specific statistical properties of the k-th output.

In contrast, the multi-output GP models the joint distribution over all six output dimensions by treating $\mathbf{y}(\mathbf{q}) \in \mathbb{R}^6$ as a vector-valued GP:

$$\mathbf{y}(\mathbf{q}) \sim \mathcal{GP}(\mathbf{m}(\mathbf{q}), \mathbf{K}(\mathbf{q}, \mathbf{q}')), \tag{4.2}$$

where $\mathbf{m}(\mathbf{q}) \in \mathbb{R}^6$ is a vector-valued mean function and $\mathbf{K}(\mathbf{q}, \mathbf{q}') \in \mathbb{R}^{6 \times 6}$ is a matrix-valued kernel function encoding both spatial similarity (via $\mathbf{q}, \mathbf{q}'$) and input-output correlations.

For this work, we opted for the single-output approach, training six independent GPs, each predicting one output feature in $\mathbf{y}$ (see Figure 4.1). It is important to note that each sub-model can have different hyperparameters. This approach maintains numerical stability, as one underlying process of GPR directly involves the inversion of the covariance matrix, while achieving a reasonable predictive accuracy across all output dimensions (see Section 4.1.2). Moreover, the individual components (α_k, β_k) correspond to distinct mechanical metrics derived from different spatial measurements. As such, assuming negligible input-output correlations is reasonable and further justifies our modelling choice.
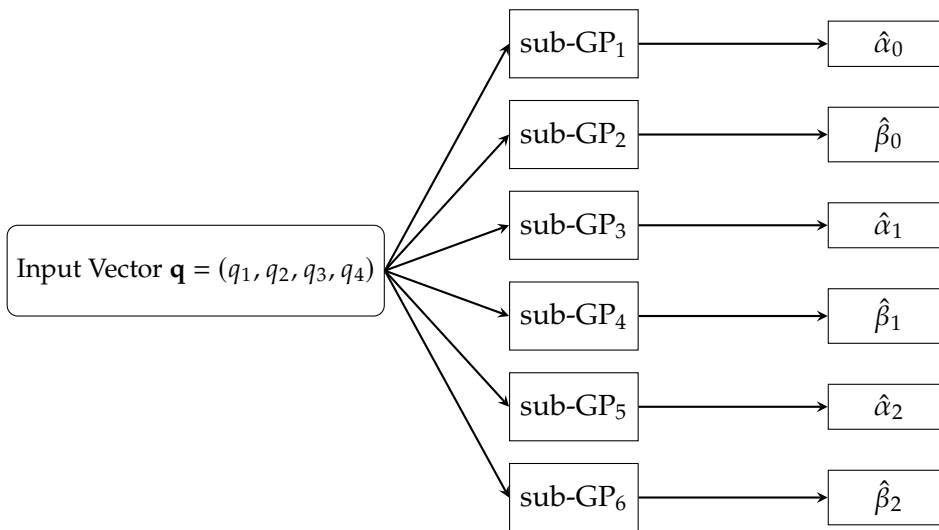
Figure 4.1: Schematic representation of the adopted single-output GP framework. Each component of the output vector $\mathbf{y} = (\alpha_0, \beta_0, \alpha_1, \beta_1, \alpha_2, \beta_2)$ is predicted using an independently trained GP model. Based on [34].

23

Alternative regression models could also be considered for emulating the forward model. For instance, Cai et al. [34] explored three different techniques: K-nearest neighbors (KNN), XGBoost, and multi-layer perceptron (MLP) in a similar biomechanical context and reported very accurate results. Among them, XGBoost achieved the highest predictive accuracy for modelling LV diastolic dynamics and estimating underlying material parameters. These models, however, are inherently deterministic, as they provide point predictions without a measure of confidence, and lack the ability to incorporate prior knowledge about the problem structure.

In contrast, GPs offer a fully Bayesian probabilistic framework. This comes with two major advantages: first, the model outputs are not just predictions but full predictive distributions, which are essential for quantifying uncertainty; and second, the model is flexible in encoding prior beliefs through the covariance function, the choice of which is a fundamental step in formulating a GP framework. This probabilistic nature is especially advantageous in parameter inference, where multiple combinations of inputs **q** may lead to similar mechanical behavior. A GP framework allows us to assign probabilities to such mappings.

Furthermore, the ability to quantify uncertainty is critical in clinical applications, where decisions rely not only on the accuracy of predictions, but also on knowing how confident the model is in those predictions, making GPs a more suitable surrogate modelling tool for the context explored in this thesis.

4.1.2 Predictive Performance

The trained emulator achieved high predictive accuracy across all six output components. Table 4.1 summarizes the MSE and R^2 values computed on the test set. The values indicate excellent agreement between the emulator's predictions and the ground-truth simulation outputs, with R^2 scores consistently exceeding 0.98. Therefore, it is safe to conclude that the surrogate model accurately captures the LV dynamics.

Table 4.1: Predictive performance metrics for each output component on the held-out test set.

Parameter	MSE	R^2
α_0	0.0022	0.9999
β_0	0.0001	0.9984
α_1	26.5420	0.9867
β_1	0.0005	0.9839
α_2	1.2204	0.9974
β_2	0.0002	0.9943

To further illustrate model performance, Figure 4.2 shows scatter plots comparing predicted values against true values for each output variable.
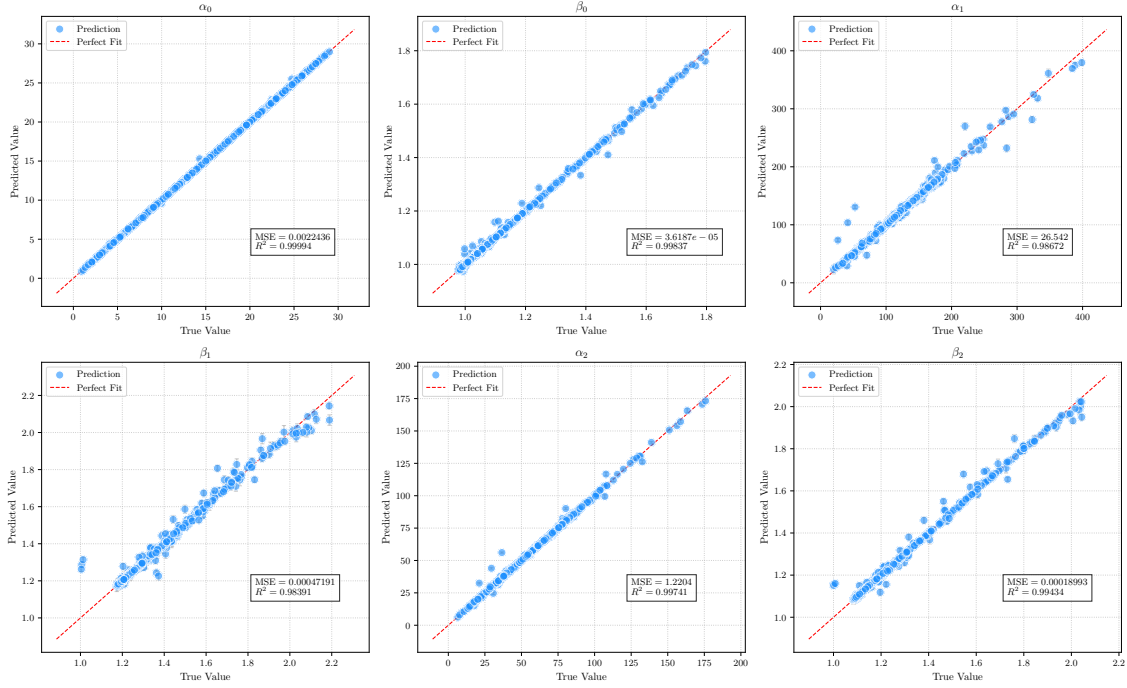
Figure 4.2: Predicted vs. true values for each output component in the test set. The dashed diagonal line indicates the perfect fit.

While there remains some variability, particularly in the prediction of α_1, the performance of the emulator is still well within plausible limits for the problem at hand. As shown in both Table 4.1 and Figure 4.2, α_1 does have a significantly larger prediction error. This is partially explained by the larger absolute size of this feature. The mean value of α_1 (≈ 123) is significantly larger than that of the other features, which typically fall below 60. Because the mean squared error (MSE) is sensitive to the magnitude of the output values, even small relative deviations in high-mean features can result in larger absolute errors. Therefore, the elevated MSE observed for α_1 does not necessarily imply poorer performance, but rather reflects its broader output range. This is further confirmed by the value of R^2, which is a scale-independent metric: for α_1, the R^2 remains comparable to that of the other features, confirming that the emulator captures the relative variability of this output with a similar degree of confidence when compared to other features that perform better in a scale-dependent evaluation metric, such as the MSE.

4.2 Sensitivity Analysis

To naturally understand the need for sensitivity analysis (SA), it is important to step back and analyze the structure of a generic computational model. Initially, a model is defined by its structure (the states of variables and the possible transitions among them), then by the rates at which those variables develop (whether they increase, decrease, or remain constant), then by the functional dependence of those rates (time-invariant or time-varying, density-independent or density-dependent, deterministic or stochastic), and finally by

25

the numerical values assigned to the parameters that define the rates [38]. A set of any parameters operating within a given model generates the outcomes calculated from the model, whether that is population growth rate, structural deformation, or biomechanical response. The core idea of SA is to determine how changes in these parameters influence the model outputs, either through single-parameter variation (local sensitivity analysis (LSA)) or through global assessment over a distribution of inputs (global sensitivity analysis (GSA)).

While SA is not mandatory for building a predictive framework, it is valuable as a complementary step when the problem context requires deeper interpretability. In the present case, the development of a surrogate model for passive diastolic filling of the LV motivates SA for two reasons. First, it allows exploration of how physiological changes such as fibrosis, loss of compliance, or altered myocardial contractility affect the biomechanical quantities of interest (QoIs), i.e., our simulated output features **y**. Second, SA provides a broader understanding of how outcomes are determined in complex systems, particularly in nonlinear settings [45].

Due to the nonlinearity and anisotropy of myocardial tissue, small variations in material parameters can yield disproportionately large effects on model predictions. Therefore, SA is a valuable approach for quantifying such effects.

This chapter intends to provide a mathematical foundation for the SA implementation and to describe how both GSA and LSA were used to understand relevant associations between input parameters and output features.

4.2.1 Global Sensitivity Analysis

GSA is a subset of SA where input parameters are varied across their full distribution, simultaneously. It's a very common technique for nonlinear systems. Variance based methods are a specific class of GSA methods that assess how input uncertainty contributes to output variance. These methods decompose the total variance of the output into portions attributable to each input [46].

The foundation of variance-based SA lies in the functional analysis of variance (ANOVA) decomposition, originally introduced by Sobol [47] and later formalized by Stone [48] for high-dimensional models. From a black-box[1] perspective, any model can be represented as a function $y = f(\mathbf{q})$, where $\mathbf{q} = (q_1, \ldots, q_n)$ is a vector of uncertain input variables defined over a domain $\mathbb{G} \subset \mathbb{R}^n$, and $y \in \mathbb{R}$ is a scalar output. Without reproducing the full derivation (see [47, 49, 50] for details), the result is a variance decomposition of the form

$$\mathbb{V}\mathrm{ar}(y) = \sum_{i=1}^{n} V_i + \sum_{i<j} V_{ij} + \sum_{i<j<k} V_{ijk} + \cdots + V_{1,\ldots,n}, \tag{4.3}$$

---

[1]A black-box is a system which can be viewed in terms of its inputs and outputs, without requiring knowledge of its internal workings.

where $V_i = \mathbb{V}\mathrm{ar}_{q_i}[\mathbb{E}_{q_{\sim i}}(y \mid q_i)]$, $V_{ij} = \mathbb{V}\mathrm{ar}_{q_{ij}}[\mathbb{E}_{q_{\sim ij}}(y \mid q_i, q_j)] - V_i - V_j$, and so forth. The $q_{\sim i}$ notation indicates the set of all variables except q_i. Together, all variance terms must sum to the total variance of the model output.

The first-order Sobol index S_i measures the individual contribution of input q_i to the output variance, excluding any interactions with other inputs:

$$S_i = \frac{V_i}{\mathbb{V}\mathrm{ar}(y)} = \frac{\mathbb{V}\mathrm{ar}_{q_i}[\mathbb{E}_{q_{\sim i}}(y \mid q_i)]}{\mathbb{V}\mathrm{ar}(y)}. \tag{4.4}$$

This index captures how much of the output variability can be explained by varying q_i alone, keeping all other inputs fixed. It is standardised by the total variance to provide a fractional contribution.

Moreover, when two or more parameters jointly affect the output in a way that cannot be attributed to any of them individually, interaction terms must be considered. For instance, the second-order index S_{ij} quantifies the variance contribution of the interaction between q_i and q_j:

$$S_{ij} = \frac{V_{ij}}{\mathbb{V}\mathrm{ar}(y)} = \frac{\mathbb{V}\mathrm{ar}_{q_{ij}}[\mathbb{E}_{q_{\sim ij}}(y \mid q_i, q_j)] - V_i - V_j}{\mathbb{V}\mathrm{ar}(y)}. \tag{4.5}$$

Though higher-order indices ($S_{ijk}, S_{ijkl}, \ldots$) are theoretically well-defined, their calculation is usually infeasible for generic models, as it requires the evaluation of $2^n - 1$ indices, which can become computationally expensive.

Finally, the total Sobol index S_{T_i} captures the full contribution of input q_i, including both its main effect and all interactions involving q_i:

$$S_{T_i} = 1 - \frac{\mathbb{V}\mathrm{ar}_{q_{\sim i}}[\mathbb{E}(y \mid q_{\sim i})]}{\mathbb{V}\mathrm{ar}(y)}, \tag{4.6}$$

This index is particularly useful for identifying variables that are influential through interactions even if their first-order effects are small.

4.2.1.1 GSA Results

The results of the GSA are presented below. Table 4.2 shows the first-order and total-order indices for every input parameter $\mathbf{q} = (q_1, q_2, q_3, q_4)$ across all six output features $\mathbf{y} = (\alpha_0, \beta_0, \alpha_1, \beta_1, \alpha_2, \beta_2)$. while Figure 4.3 provides a visual overview of both S1 and ST indices for each output.

Table 4.2: First-order (S1) and total-order (ST) Sobol indices for each input parameter q_i and output feature y_j.

Input	α_0		β_0		α_1		β_1		α_2		β_2	
	S1	ST	S1	ST	S1	ST	S1	ST	S1	ST	S1	ST
q_1	0.34	0.35	0.10	0.22	0.59	0.80	0.03	0.06	0.62	0.84	0.01	0.05
q_2	0.66	0.66	0.79	0.91	0.20	0.41	0.93	0.96	0.16	0.38	0.96	0.98
q_3	0.00	0.00	0.00	0.00	0.00	0.00	0.00	0.01	0.00	0.00	0.00	0.00
q_4	0.00	0.00	0.00	0.00	0.00	0.01	0.01	0.03	0.00	0.00	0.01	0.02
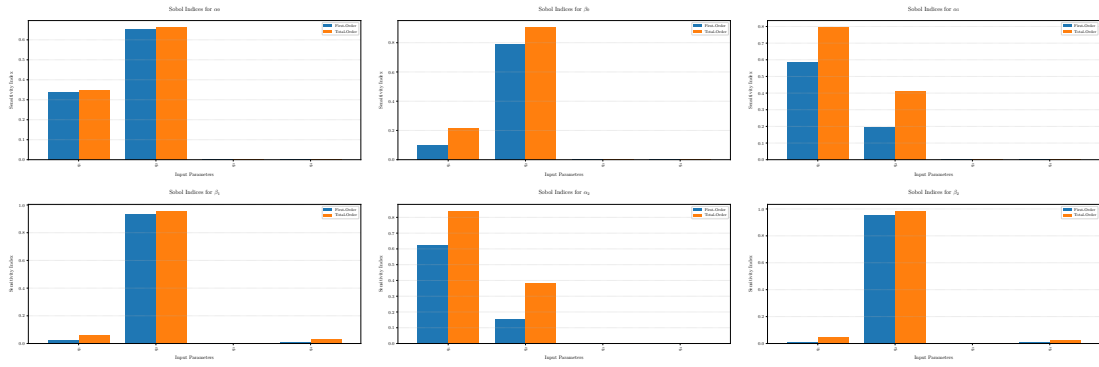
Figure 4.3: First-order (S1) and total-order (ST) Sobol indices for each input parameter across the six output features.

The observed differences between S1 and ST indices, particularly in features such as β_0, α_1 and α_2 show that interactions between parameters can have non-negligible influence in output variance. These results are further discussed in Section 4.2.3.

4.2.2 Local Sensitivity Analysis

LSA follows the same idea of GSA, but with a slight difference. While GSA tends to explore the contribution of input variability across the entire input space, LSA focuses on understanding how small perturbations around a specific baseline point affect model output [51]. Essentially this means that LSA evaluates the gradient of the model response with respect to each input parameter, assuming other inputs are held constant. This means that for a scalar model output $y = f(\mathbf{q})$, where $\mathbf{q} = (q_1, q_2, q_3, q_4)$, local sensitivities are captured via partial derivatives [52] as

$$\frac{\partial y}{\partial q_i}\bigg|_{\mathbf{q}=\mathbf{q}_0}, \tag{4.7}$$

where $\mathbf{q}_0$ is a fixed baseline input vector. This method is particularly valuable for detecting local trends and/or inflection behavior in the output response. However, Tang et al showed that if the model is nonlinear, the results of LSA can be heavily biased, as they are strongly influenced by independence assumptions and a limited exploration of model inputs [53]. Moreover, when interactions between input parameters are non-negligible,

LSA will underestimate their contribution, as it does not account for joint effects [54]. In general, as LSA only partially and locally explores a model's parametric space, it is not suitable as a standalone approach for nonlinear systems [55]. Nevertheless, it still remains a valuable tool and should be interpreted as complementary to GSA, providing more specific information in a region of interest.

4.2.2.1 LSA Results

Figure 4.4 shows the resulting sensitivity curves for both q_1 and q_2. Perturbations of q_1 and q_2 produced clear changes in the outputs, while q_3 and q_4 had negligible influence and are therefore omitted for simplicity.

(a) q_1 – impact on α outputs   **(b)** q_1 – impact on β outputs

(c) q_2 – impact on α outputs   **(d)** q_2 – impact on β outputs
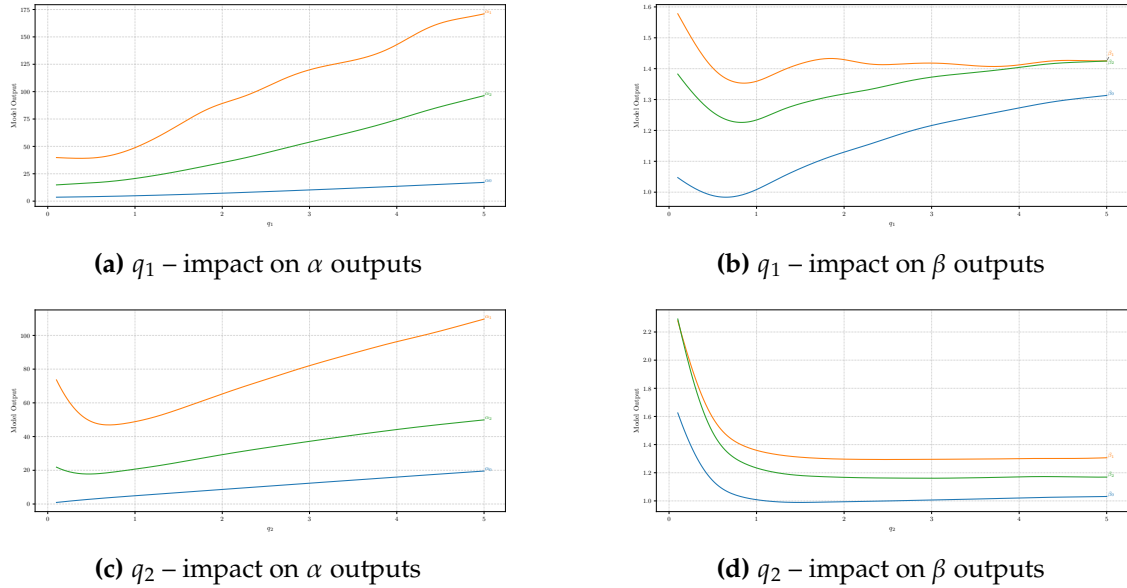
Figure 4.4: Univariate local sensitivity analysis for the two influential parameters.

4.2.3 Interpretation

The results from both SA approaches are in strong qualitative agreement, with only minor inconsistencies. From Table 4.2, one can safely consider both q_3 and q_4 to have a negligible effect, as their first-order and total-order Sobol indices are consistently near zero, and the LSA sweep plots further confirm that by showing flat responses across every output feature. This insensitivity can be justified by revisiting the form of the strain energy function used to model passive myocardial tissue (see Equation (2.5)). Parameters q_3 and q_4 correspond to directions orthogonal to the predominant fibre alignment, typically associated with transverse or shear stiffness components, and their influence in diastolic deformation, particularly under physiological loading, is limited. Since the passive diastolic mechanics are governed mainly by stiffness along the fibre and sheet directions, the role of the corresponding material parameters is reduced, especially in short-axis projections of end-diastolic shape from which the output features are derived.

By contrast, q_1 and q_2 are dominant. The S1 indices for q_1 show clear contributions to the variance of α_0, α_1, and α_2, but little effect on the β features. Interaction effects further amplify its role in α_1 and α_2, consistent with the LSA results where varying q_1 produces sharp changes in α outputs but flat responses in β. This can be explained by the fact that q_1 primarily controls the stiffness along the fibre direction, which in turn dominates the principal stretch modes captured by the α parameters.

The most influential parameter is, by far, q_2, as shown by its S1 and ST indices in Table 4.2, often approaching or exceeding 0.9. It determines nearly the entirety of the variance in β_0, β_1, and β_2, and plays a major role in α_0, α_1, and α_2 as well, either through individual contributions or through interactions with other parameters, as indicated when ST > S1. The high sensitivity associated with q_2 can be explained by analyzing its possible role in the system. Physiologically, q_2 likely governs stiffness in the sheet or sheet-normal direction, which affects transverse wall expansion and introduces coupling in volumetric deformation. Its dominance can also be attributed to its role in the exponential terms of the strain energy function, where small perturbations in q_2 may lead to disproportionately large changes in stress. This response makes q_2 the main responsible for the nonlinear behaviour of the system.

Finally, one can use the results obtained from both GSA and LSA to draw relevant insights regarding not only the responses of the model as a whole, but also the behaviour of the parameters that determine those responses. First and most evidently, we can assume q_3 and q_4 as practically inactive in this modelling scenario. Secondly, q_1 appears to influence outputs primarily along the fibre direction, i.e., the longitudinal direction, as evidenced by its effect on α parameters. Thirdly, q_2 is globally dominant across all features, confirming its exponential scaling effect on myocardial stiffness during diastolic filling. Finally, interaction effects are not negligible and must be taken into consideration, particularly if an hypothetical perturbation affects either q_1 or q_2. These conclusions confirm that priority should be given to the control of q_1 and q_2, while q_3 and q_4 could potentially be fixed in the inference phase, described in the next section.

4.3 Parameter Inference

Parameter inference is a subset of statistical inference that involves estimating the parameters of a mathematical model from observed data [56]. In the context presented throughout this work, this means capturing real-time cardiac behaviour, specifically during the diastolic filling of the LV, and assign a set of plausible parameters to such behaviour. The inferred parameters correspond to myocardial tissue properties that are otherwise inaccessible through non-invasive procedures. The underlying idea is to identify a set of plausible parameters $\mathbf{q} = (q_1, q_2, q_3, q_4)$ such that the model's predicted response $f(\mathbf{q})$ closely matches the observed mechanical behavior $\mathbf{y}_{\text{obs}}$, obtained via magnetic resonance imaging (MRI) or computed tomography (CT) scans. This proximity is evaluated through

a distance function that will determine whether the proposed sample is close enough to the observed data in order to be accepted [57].

This problem can be approached using both deterministic and probabilistic frameworks. In the deterministic setting, a single point estimate is sought by minimizing a cost function quantifying the discrepancy between the model output and the observations. In contrast, the Bayesian approach treats the parameters as random variables and computes their posterior distribution conditioned on the data.

In this work, we pursued both approaches and compared them against each other to assess both estimation accuracy and computational cost. This section focuses on how those approaches were implemented. Initially, we formulate the inverse problem associated with estimating myocardial material parameters during passive diastolic filling of the LV, followed by two resolution strategies: a deterministic solution based on a global optimization method for point estimation, and a probabilistic solution using Markov chain Monte Carlo (MCMC) sampling for posterior inference. Finally, we evaluate the implications of these results in the context of uncertainty quantification.

4.3.1 Inverse Problem

Inverse problems are defined, as the term itself clearly indicates, as the inverse of forward problems. Such definition is empty unless we define the concept and the context of a forward problem. Chapter 2 describes the formulation of the forward problem adopted in this work. The idea is to determine the effects based on known causes,i.e., given a system and a set of inputs, the forward problem involves predicting the outputs. In contrast, the inverse problem intends to determine the causes of a particular known effect, i.e., given a system and a set of outputs, the inverse problem involves predicting the inputs. The solution of an inverse problem can take multiple forms, which can be roughly classified depending on their outcome [58]. The most straightforward solution is the point estimate, that essentially answers the question *"Given some observed data, y_{obs}, and the prior information, what is the most probable value of the unknown* $\mathbf{q}$*?"*. Point estimates rely on either variational or sequential methods [59]. Both methods provide optimal least-squares estimates by minimizing a cost function accounting for the misfit between measured data and state observations. This solution, although relatively simple and accurate, doesn't account for the intrinsic ill-posedness of an inverse problem. As stated by Jacques Hadamard [60], a problem involving the modelling a physical process through PDEs is said to be well-posed if:

(I) There exists at least one solution (existence).

(II) There is at most one solution (uniqueness).

(III) The solution depends continuously on data (stability).

The forward problem is assumed to be well-posed. The inverse problems are generally ill-posed and often violate at least one of the above conditions. To address the intrinsic ill-posedness of inverse problems, we adopted an alternative method to obtain the solution of our inverse problem based on confidence regions. Essentially, this method yields the possibility of characterizing the probability distribution of the unknown parameters provided they are described in terms of random variables. Rather than obtaining a single point estimate for the input parameters, this method attempts to remove ill-posedness by restating the inverse problem as a well-posed extension in a larger space of probability distributions, meaning it produces a distribution that can be used to obtain estimates that, loosely speaking, have different probabilities [61]. Hence, this approach answers questions like *"In what interval are the values of the unknown with 90% probability, given the prior and the data?"*.

The next sections will present the concrete implementation of both the deterministic and probabilistic approaches used in this work, along with the results for each of them.

4.3.2 Point Estimation via Global Optimization

For the point estimate solution, we adopted a direct approach based on a deterministic framework. The idea is to compute a single point estimate for the parameter vector $\mathbf{q} \in \mathbb{R}^4$ that minimizes the discrepancy between the model prediction $\hat{\mathbf{y}}(\mathbf{q})$ and the observed data $\mathbf{y}_{\text{obs}}$. This process can be formulated as:

$$\mathbf{q}^* = \underset{\mathbf{q} \in Q}{\operatorname{argmin}} \; \mathcal{L}(\mathbf{q}) = \underset{\mathbf{q} \in Q}{\operatorname{argmin}} \; \|\hat{\mathbf{y}}(\mathbf{q}) - \mathbf{y}_{\text{obs}}\|^2 , \tag{4.8}$$

where $Q \subset \mathbb{R}^4$ is the allowed domain for the parameters and $\mathcal{L}(\mathbf{q})$ denotes the loss function, here chosen as the MSE between predicted and observed outputs.

For the global optimization, we employed the DE algorithm, first introduced by Storn et al. DE is a stochastic direct search method that iteratively perturbs candidate solutions via weighted differences of random population member [62]. It is normally used for multidimensional functions but does not use the gradient of the problem being optimized, which means DE does not require the optimization problem to be differentiable [63], as is required by multiple optimization methods such as gradient descent, making DE a suitable choice for this context.

4.3.2.1 Results

To have an idea of how precise the inference process was, a validation point was withdrawn from the dataset exclusively for this purpose. This point was not used to train or test the model. This way, we were able to assess the accuracy of the inferred parameters by comparing them against the validation point. Moreover, for each parameter q_i, the best estimate was selected individually based on the smallest absolute error across runs. The results are summarized on Table 4.3.

Table 4.3: Best per-component estimates from differential evolution.

Parameter	Estimate	True Value	Abs. Error	Run ID
q_1	4.5018	4.5003	0.0015	6
q_2	3.5894	3.5885	0.0009	34
q_3	3.8222	3.8925	0.0703	26
q_4	3.5280	3.5079	0.0201	13

It is important to note the unrealistic nature of the validation point, used purely as a comparison factor. In a real clinical context, such validation point does not exist, as it corresponds to the unknown point we are trying to estimate. Figure 4.5 shows the loss evolution of the minimization process throughout the 50 runs of the algorithm.
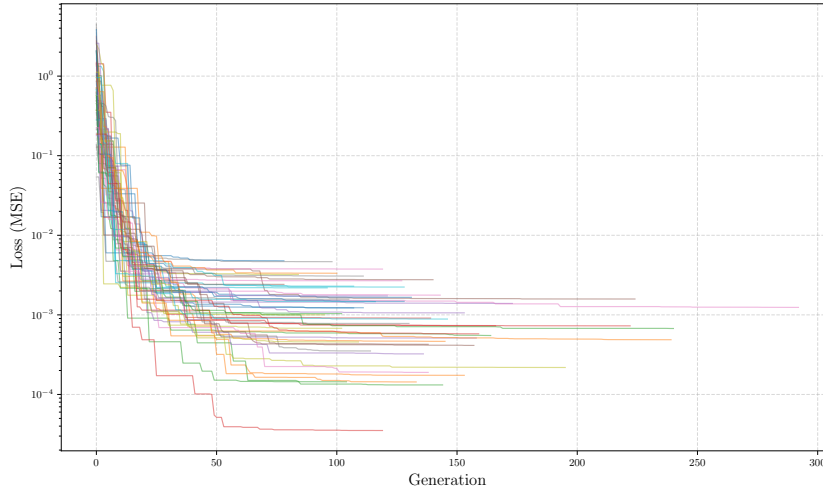
Figure 4.5: Loss evolution across 50 independent DE runs. Despite stochasticity, most runs converge below a target loss within 100 iterations.

4.3.3 Bayesian Inference via MCMC

The probabilistic inference approach adopted in this work follows Bayes' theorem [64]. Generally speaking, we start by choosing a probability density $\pi(\theta)$ that expresses our beliefs about a parameter θ before we see any data, called the prior distribution and represented by the covariance function. We then choose a statistical model $p(x|\theta)$ that reflects our beliefs about x given θ. After observing data $\mathbb{D}_n = X_1, \ldots, X_n$, we update our beliefs and calculate the posterior distribution $p(\theta|\mathbb{D}_n)$. Mathematically, the posterior distribution can be written as

$$p(\theta|X_1, \ldots, X_n) = \frac{p(X_1, \ldots, X_n|\theta)\pi(\theta)}{p(X_1, \ldots, X_n)} = \frac{\mathcal{L}_n(\theta)\pi(\theta)}{c_n} \propto \mathcal{L}_n(\theta)\pi(\theta), \quad (4.9)$$

where $\mathcal{L}_n(\theta) = \prod_{i=1}^{n} p(X_i|\theta)$ is the likelihood function and

$$c_n = p(X_1, \ldots, X_n) = \int p(X_1, \ldots, X_n|\theta)\pi(\theta)\, d\theta = \int \mathcal{L}_n(\theta)\pi(\theta) d\theta \quad (4.10)$$

is the normalizing constant, also known as marginal likelihood. In our setup, the likelihood is constructed from the trained GPs models, where each one of them provides a probabilistic prediction of the system outputs given θ. From a pure Bayesian viewpoint, the posterior distribution represented in Eq. 4.9 is the complete answer to the question: *What is the value of θ?* However, in many applications, including the one being studied here, it is still advantageous to have a single estimate $\hat{\theta}$, as well as an interval describing our uncertainty about θ. For this purpose, we computed the posterior mode of each inferred parameter, also known as maximum a posteriori (MAP) estimation:

$$\hat{\theta}_{\text{MAP}} = \underset{\theta}{\text{argmax}} \left[\mathcal{L}_n(\theta)\pi(\theta) \right]. \tag{4.11}$$

Essentially, this metric selects the maximum value of the distribution, i.e., the most probable value under the posterior. Alternatively, one could also use the posterior mean, which is given by the mean value of the distribution and minimizes the squared error and can be defined as

$$\bar{\theta}_n = \int \theta p(\theta|\mathbb{D}_n)d\theta = \frac{\int \theta \mathcal{L}_n(\theta)\pi(\theta)d\theta}{\int \mathcal{L}_n(\theta)\pi(\theta)d\theta}. \tag{4.12}$$

Since it can also be an insightful metric, it was equally computed. However, and because the posterior distributions obtained for q_3 and q_4 showed a low degree of identifiability, we found the mode to better represent the distribution when compared to the mean (particularly as the latter is not guaranteed to fall on a value actually obtained in the sample), hence being the metric that should mostly be taken into consideration when interpreting the results.

In addition to point estimates, we report 95% Bayesian credible intervals derived from the marginal posterior distributions.

4.3.3.1 Results

The results obtained completely validate Section 4.2, consequently validating our uncertainty propagation approaches both for the forward and inverse problems. Figure 4.6 shows the calculated posterior distribution for each parameter $\mathbf{q} = (q_1, q_2, q_3, q_4)$, as well as the mean and mode of that distribution paired with the true value withdrawn from the validation point. Finally, a 95% credible interval is also represented.
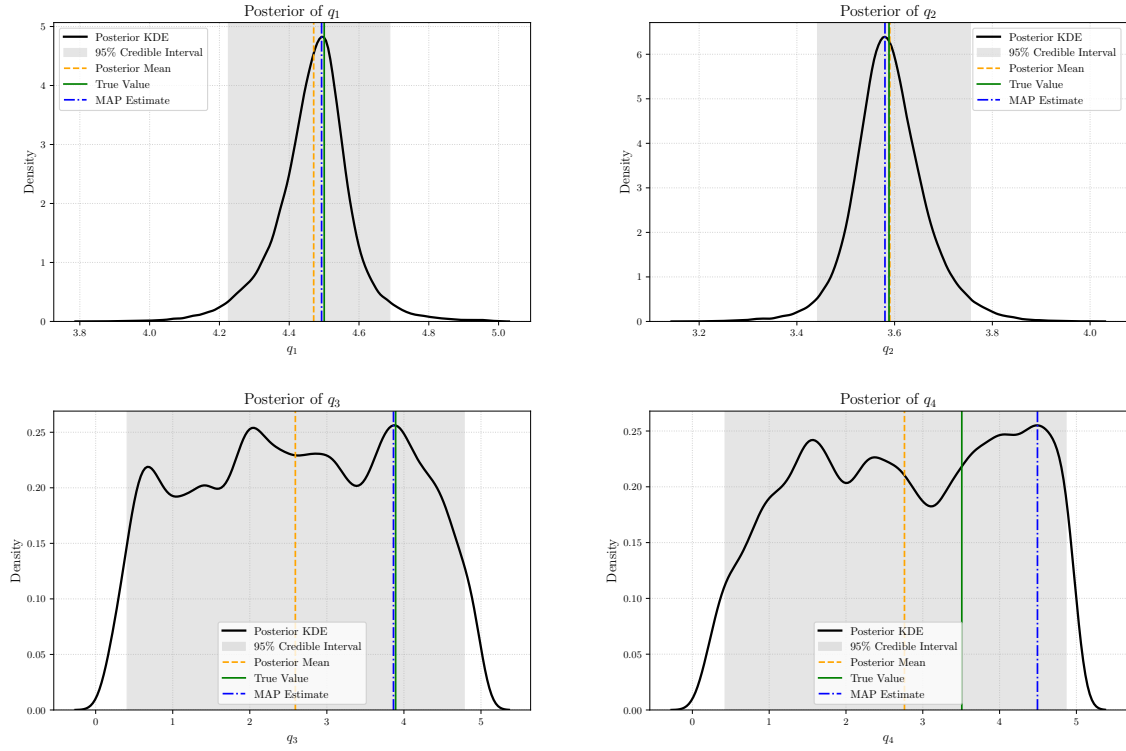
Figure 4.6: Marginal posterior distributions of inferred parameters

The posterior distributions in Figure 4.6 show a clear difference between the first two parameters and the latter ones. Both q_1 and q_2 exhibit well-defined distributions centered around the MAP estimate, indicating that these parameters are strongly identifiable from the available data. In contrast, the posteriors for q_3 and q_4 are irregular, without a clear peak. This behavior reflects an identifiability problem, as the model outputs are less sensitive to changes in these parameters, so the data do not provide enough information to constrain their values. These findings are consistent with the results of the SA carried in Section 4.2, which showed that q_3 and q_4 contribute less to the output variance, and the wide posteriors captured by the Bayesian framework confirm this through explicit uncertainty.

4.4 Uncertainty Quantification

Model personalization refers to the adaptation of model inputs to subject-specific conditions, which may be even more important than the model itself, especially in the context of this work. To move towards model personalization means to address inevitable obstacles that may prevent us from achieving that goal. Understanding the dynamics between the sensitivity of model predictions to errors and uncertainties in the model inputs then becomes one fundamental issue that must be approached carefully. These inputs may include the geometry of the domain (e.g., vascular networks), physical properties (e.g., material parameters), and boundary conditions. Due to biological variability and measurement

noise, uncertainty in these inputs is unavoidable.

Furthermore, Section 4.3 is of most importance precisely because not all model inputs are directly measurable, thus amplifying the need to solve parameter estimation problems. The uncertainties carried by patient-specific features should then be incorporated into the computational model, to quantify their impact on the computed results and to obtain more reliable predictions or best/worst-case scenarios [65].

Typically, uncertainty quantification (UQ) problems involve a mathematical model for a process of interest, subject to some uncertainty about the correct form of this model or, more frequently, about some of its parameters [66]. While closely related to parameter estimation and data assimilation, UQ problems also involve the propagation of uncertainty on outputs of interest, reliability analysis or certification problems, prediction problems and, very often, consist of several of these aspects coupled together. For instance, after estimating some model parameters, we may use them to forward-propagate other uncertainties. Often, though not always, uncertainty is modeled in a probabilistic framework, thus requiring probabilistic and statistical methods.

This section describes how we accounted for uncertainty, particularly focusing on basic aspects related to both forward propagation and inverse propagation of uncertainty.

4.4.1 Forward Uncertainty

The goal of forward UQ is to derive information about the uncertainties in system outputs of interest, given information about the uncertainties in the system inputs. The goal is to obtain the probability density function (PDF) of some QoIs given the probability distribution of the input $\mathbf{q} = (q_1, q_2, q_3, q_4) \in \mathbb{R}^4$, or evaluate statistical measurements (e.g. the expected value and the variance), correlation functions, confidence regions or quantiles.

Multiple techniques have been employed in order to accurately propagate uncertainties through models. Because those models usually exhibit nonlinear parameter dependencies, linear parameterized models arose in applications such as X-ray tomography, image processing and acoustic phenomena [67–69]. Another common employed strategy is based on sampling methods, mainly used in applications where distributions for measurement errors and input uncertainties have been previously determined, particularly by initial or boundary conditions [70, 71]. Perturbation methods are another, yet less common technique to propagate uncertainty. These methods are based on truncated Taylor expansions of the model response or QoIs evaluated at parameter mean [72]. Spectral representations are also a well defined method for the task considered. The underlying idea is to represent uncertain outputs in a manner that facilitates the evaluation of moments and distributions for the QoIs [73]. This is achieved by employing spectral expansions that exploits the smoothness, often associated with high-dimensional parameter spaces, to improve the convergence of techniques used to specify QoIs [74].

Among the several techniques available, this work adopts a SA approach, both local

and global, the results of which are presented in Section 4.2. While SA doesn't directly offer a complete probabilistic UQ framework, it still may be seen as a precursor of forward UQ, providing a quantitative description of the dependence of the solution of a model on input parameters, and helps prioritize which of those parameters should be more precisely characterized. Donders et al. managed to apply a SA-based approach to a pulse wave propagation model of arterial flows [75]. Section 4.2.3 provides a detailed interpretation of the results achieved in both SA, which can be directly linked to an uncertainty-based perspective. The varying degrees of output sensitivity to individual inputs indicate that certain parameters must be carefully calibrated, as even small perturbations can lead to significant deviations in model predictions, whereas others may have negligible impact.

4.4.2 Inverse Uncertainty

Inverse UQ, also known as backward uncertainty propagation, refers to the process of inferring uncertain model inputs from a specific set of observed outputs. In this work, both deterministic and probabilistic formulations were explored and described thoroughly in Section 4.3. The deterministic approach relies on variational methods, where point estimates for the unknown inputs $\mathbf{q} = (q_1, q_2, q_3, q_4)$ were obtained by minimizing a suitable loss function (MSE in our case) through a metaheuristic[2] optimization algorithm called differential evolution. This particular approach results in a single-value estimate, useful in practice but limited in terms of uncertainty characterization, which becomes fundamental when the goal is model personalization.

To overcome these intrinsic limitations, a Bayesian inference framework was adopted to statistically quantify the uncertainty associated with the estimated inputs. In this setting, the unknown parameters are treated as random variables, and the solution to the inverse problem becomes the posterior distribution of the inputs conditioned on observed data (See Eq. 4.9). By employing `emcee`, we generated posterior samples that represent the full distribution of plausible input configurations. This enables not only the computation of point estimates in the final phase of the procedure (e.g., MAP or posterior mean), but also the calculation of Bayesian credible intervals, which provide probabilistic bounds on the inferred quantities. In our case, we constructed a 95% credible interval. This means that given the observed data and our prior beliefs, we can confidently state that there is a 95% probability that the true value of the unknown parameter lies within that specific interval. This probabilistic perspective allows a more comprehensive understanding of input uncertainty, particularly in situations where direct measurements are unavailable, incomplete or flawed.

---

[2]Metaheuristics refers to a stochastic optimization procedure that makes few or no assumptions about the optimized problem.

5

Discussion

This thesis explored statistical emulation as a strategy to overcome the prohibitive computational costs of cardiac finite element simulations. Whereas full parameter estimation based on the Holzapfel–Ogden law remains too expensive for routine use, the proposed GP framework replaces the forward model with a fast surrogate. The results obtained in this thesis show that the emulator accurately replicates the behaviour of a cardiac model with negligible loss of accuracy, while reducing computational requirements by a large factor. On average, evaluating all six output components for a new input vector $\mathbf{q}$ takes around 5 milliseconds, representing a difference of over 5 orders of magnitude when compared to the original simulator. This is the main advantage of using an emulator in situations where repeated forward evaluations are necessary and efficiency must be taken into account.

Nevertheless, several limitations need to be acknowledged. The current framework was trained on simulations of a simplified LV geometry and only considered the passive diastolic filling phase. Active contraction and electromechanical coupling remain outside the present scope, yet they are essential for a complete description of cardiac dynamics. In addition, the scalability of GPs remains a challenge, as the cubic complexity in the number of training points restricts extensions to larger parameter spaces. Finally, the model assumes a fixed fibre architecture, ignoring individual variability. Ideally, and since the long-term goal is to develop patient-specific emulators, one should account for variations in myofibre structure across individuals. While advancements have been made in this direction [76, 77], incorporating such features into emulation pipelines is not yet feasible [78].

Therefore, the work developed in this thesis demonstrates how GPs can act as statistical surrogates for computationally expensive biomechanical simulations. To extend this to clinical translation, emulators need to incorporate realistic variations in ventricular geometry and material properties, including those induced by pathological changes such as fibrosis or infarction. SA and dimension reduction techniques could help identify low-dimensional parameterizations, making the approach scalable to more developed models.

Future work should investigate scalable extensions such as sparse or deep GPs, capable

of handling higher-dimensional spaces. Automatic kernel construction should also be explored, as it allows the kernel to perfectly captures the mechanical behaviour of an individual's LV, removing the generalization of one-size-fits-all. Additionally, integration with medical imaging pipelines could enable the personalization of emulators directly from MRI-derived anatomical and microstructural data. The feasibility of such extensions should make it possible to deploy statistical emulators as part of real-time diagnostic tools.

Overall, this thesis sets the foundation for efficient emulation of cardiac mechanics. By replacing expensive simulations with fast surrogates, we are able to create an accurate framework with integrated uncertainty capable of recovering material parameters without directly accessing the heart or any of its components. This framework provides a factor of interpretability by quantifying confidence in the results. In doing so, it brings cardiac modelling one step closer to clinical applicability.

6

CONCLUSION

In this thesis, we have developed and evaluated a statistical emulation framework for cardiac mechanics, focusing on the passive filling phase of the LV. By leveraging GPR with an appropriate kernel, we demonstrated that it is possible to replace computationally expensive finite element simulations with fast, accurate surrogates that preserve both predictive accuracy and uncertainty quantification.

The core contribution of this work is the construction of six GPs regressors emulating the key outputs of the cardiac simulator, accurately reproducing the behaviour of the LV during passive diastolic filling across the full parameter space. This approach enables a non-invasive recovery of myocardial material parameters while offering a degree of confidence, which becomes particularly important in clinical settings. The successful application to LV dynamics validates the feasibility of using statistical emulation as a practical surrogate for complex biomechanical models.

While several challenges remain, particularly regarding scalability, incorporation of active contraction, and personalization to patient-specific fibre architectures, as previously discussed, the framework presented here establishes a solid foundation. Future extensions, such as deep or sparse GPs and integration with imaging pipelines, could enable clinically viable and real-time emulation.

In summary, this work contributes to bridging the gap between detailed biomechanical models and practical applications by providing a computationally efficient surrogate modelling strategy. By advancing the tools for fast and reliable cardiac emulation, it represents an important step toward personalized medicine.

Bibliography

[1] J. M. Lourenço. *The NOVAthesis LATEX Template User's Manual*. NOVA University Lisbon. 2021. URL: https://github.com/joaomlourenco/novathesis/raw/main/template.pdf (cit. on p. i).

[2] A. Timmis et al. "European Society of Cardiology: cardiovascular disease statistics 2021". In: *European heart journal* 43.8 (2022), pp. 716–799 (cit. on p. 1).

[3] R. Klabunde. *Cardiovascular physiology concepts*. Lippincott Williams & Wilkins, 2011 (cit. on p. 2).

[4] T. Arts et al. "Relating myocardial laminar architecture to shear strain and muscle fiber orientation". In: *American Journal of Physiology-Heart and Circulatory Physiology* 280.5 (2001), H2222–H2229 (cit. on p. 2).

[5] S. H. Gilbert et al. "Visualization and quantification of whole rat heart laminar structure using high-spatial resolution contrast-enhanced MRI". In: *American Journal of Physiology-Heart and Circulatory Physiology* 302.1 (2012), H287–H298 (cit. on p. 3).

[6] M. Misfeld and H.-H. Sievers. "Heart valve macro-and microstructure". In: *Philosophical Transactions of the Royal Society B: Biological Sciences* 362.1484 (2007), pp. 1421–1436 (cit. on p. 3).

[7] G. Sommer et al. "Biomechanical properties and microstructure of human ventricular myocardium". In: *Acta biomaterialia* 24 (2015), pp. 172–192 (cit. on p. 3).

[8] J. Wong and E. Kuhl. "Generating fibre orientation maps in human heart models using Poisson interpolation". In: *Computer methods in biomechanics and biomedical engineering* 17.11 (2014), pp. 1217–1226 (cit. on p. 3).

[9] A. K. Abbas, N. Fausto, and S. L. Robbins. *Robbins and Cotran pathologic basis of disease*. Elsevier Saunders, 2005 (cit. on p. 3).

[10] R. O. Bonow et al. *Braunwald's heart disease e-book: A textbook of cardiovascular medicine*. Elsevier Health Sciences, 2011 (cit. on p. 4).

[11] D. D. Streeter Jr and W. T. Hanna. "Engineering mechanics for successive states in canine left ventricular myocardium: I. Cavity and wall geometry". In: *Circulation research* 33.6 (1973), pp. 639–655 (cit. on p. 4).

[12] I. J. LeGrice et al. "Laminar structure of the heart: ventricular myocyte arrangement and connective tissue architecture in the dog". In: *American Journal of Physiology-Heart and Circulatory Physiology* 269.2 (1995), H571–H582 (cit. on p. 4).

[13] T. Arts et al. "Modeling the relation between cardiac pump function and myofiber mechanics". In: *Journal of biomechanics* 36.5 (2003), pp. 731–736 (cit. on p. 4).

[14] L. Geerts et al. "Characterization of the normal cardiac myofiber field in goat measured with MR-diffusion tensor imaging". In: *American Journal of Physiology-Heart and Circulatory Physiology* 283.1 (2002), H139–H145 (cit. on p. 4).

[15] K. Hayashi et al. *Computational biomechanics*. Springer, 1996 (cit. on p. 4).

[16] G. A. Holzapfel and R. W. Ogden. "Constitutive modelling of passive myocardium: a structurally based framework for material characterization". In: *Philosophical Transactions of the Royal Society A: Mathematical, Physical and Engineering Sciences* 367.1902 (2009), pp. 3445–3475 (cit. on pp. 4–6).

[17] G. Buckberg et al. "Structure and function relationships of the helical ventricular myocardial band". In: *The Journal of thoracic and cardiovascular surgery* 136.3 (2008), pp. 578–589 (cit. on p. 4).

[18] S. Nakatani. "Left ventricular rotation and twist: why should we learn?" In: *Journal of cardiovascular ultrasound* 19.1 (2011), p. 1 (cit. on p. 5).

[19] S.-J. Dong et al. "MRI assessment of LV relaxation by untwisting rate: a new isovolumic phase measure of τ". In: *American Journal of Physiology-Heart and Circulatory Physiology* 281.5 (2001), H2002–H2009 (cit. on p. 5).

[20] M. T. Maeder and D. M. Kaye. "Heart failure with normal left ventricular ejection fraction". In: *Journal of the American College of Cardiology* 53.11 (2009), pp. 905–918 (cit. on p. 5).

[21] E. McEvoy, G. A. Holzapfel, and P. McGarry. "Compressibility and anisotropy of the ventricular myocardium: experimental analysis and microstructural modeling". In: *Journal of biomechanical engineering* 140.8 (2018), p. 081004 (cit. on p. 5).

[22] S. Dokos et al. "Shear properties of passive ventricular myocardium". In: *American Journal of Physiology-Heart and Circulatory Physiology* 283.6 (2002), H2650–H2659 (cit. on p. 5).

[23] J. D. Humphrey. "Continuum biomechanics of soft biological tissues". In: *Proceedings of the Royal Society of London. Series A: Mathematical, Physical and Engineering Sciences* 459.2029 (2003), pp. 3–46 (cit. on p. 5).

[24] E. A. de Souza Neto, D. Peric, and D. R. Owen. *Computational methods for plasticity: theory and applications*. John Wiley & Sons, 2011 (cit. on p. 6).

[25]   J. Málek and E. Süli. *Modeling Biomaterials*. Springer, 2021 (cit. on p. 6).

[26]   A. Rassoli, N. Fatouraee, and R. Guidoin. "Structural model for viscoelastic proper-ties of pericardial bioprosthetic valves". In: *Artificial Organs* 42.6 (2018), pp. 630–639 (cit. on p. 6).

[27]   A. Propp et al. "An orthotropic electro-viscoelastic model for the heart with stress-assisted diffusion". In: *Biomechanics and Modeling in Mechanobiology* 19 (2020), pp. 633–659 (cit. on p. 6).

[28]   G. A. Holzapfel. *Nonlinear solid mechanics: a continuum approach for engineering science*. 2002 (cit. on pp. 6, 52, 54).

[29]   J. M. Guccione, A. D. McCulloch, and L. Waldman. "Passive material properties of intact ventricular myocardium determined from a cylindrical model". In: (1991) (cit. on p. 6).

[30]   H. Demiray. "Stresses in ventricular wall". In: (1976) (cit. on p. 6).

[31]   F. Yin. "Ventricular wall stress." In: *Circulation research* 49.4 (1981), pp. 829–842 (cit. on p. 6).

[32]   J. Humphrey and F. Yin. "On constitutive relations and finite deformations of passive cardiac tissue: I. A pseudostrain-energy function". In: (1987) (cit. on p. 6).

[33]   K. D. Costa, J. W. Holmes, and A. D. McCulloch. "Modelling cardiac mechanical properties in three dimensions". In: *Philosophical transactions of the Royal Society of London. Series A: Mathematical, physical and engineering sciences* 359.1783 (2001), pp. 1233–1250 (cit. on p. 6).

[34]   L. Cai et al. "Surrogate models based on machine learning methods for parameter estimation of left ventricular myocardium". In: *Royal Society open science* 8.1 (2021), p. 201121 (cit. on pp. 9, 12, 23, 24).

[35]   H. Gao et al. "Parameter estimation in a Holzapfel–Ogden law for healthy my-ocardium". In: *Journal of engineering mathematics* 95 (2015), pp. 231–248 (cit. on p. 9).

[36]   M. Hadjicharalambous et al. "Non-invasive model-based assessment of passive left-ventricular myocardial stiffness in healthy subjects and in patients with non-ischemic dilated cardiomyopathy". In: *Annals of biomedical engineering* 45 (2017), pp. 605–618 (cit. on p. 9).

[37]   H. Gao et al. "Changes and classification in myocardial contractile function in the left ventricle following acute myocardial infarction". In: *Journal of The Royal Society Interface* 14.132 (2017), p. 20170203 (cit. on p. 9).

[38]   R. B. Gramacy. *Surrogates: Gaussian process modeling, design, and optimization for the applied sciences*. Chapman and Hall/CRC, 2020 (cit. on pp. 11, 26).

[39] C. Currin et al. "Bayesian prediction of deterministic functions, with applications to the design and analysis of computer experiments". In: *Journal of the American Statistical Association* 86.416 (1991), pp. 953–963 (cit. on p. 11).

[40] S. Conti and A. O'Hagan. "Bayesian emulation of complex multi-output and dynamic computer models". In: *Journal of statistical planning and inference* 140.3 (2010), pp. 640–651 (cit. on p. 11).

[41] M. C. Kennedy and A. O'Hagan. "Bayesian calibration of computer models". In: *Journal of the Royal Statistical Society: Series B (Statistical Methodology)* 63.3 (2001), pp. 425–464 (cit. on p. 11).

[42] C. K. Williams and C. E. Rasmussen. *Gaussian processes for machine learning*. Vol. 2. 3. MIT press Cambridge, MA, 2006 (cit. on pp. 15–17).

[43] S. Klotz et al. "Single-beat estimation of end-diastolic pressure-volume relationship: a novel method with potential for noninvasive application". In: *American Journal of Physiology-Heart and Circulatory Physiology* 291.1 (2006), H403–H412 (cit. on p. 21).

[44] C. K. Williams and D. Barber. "Bayesian classification with Gaussian processes". In: *IEEE Transactions on pattern analysis and machine intelligence* 20.12 (1998), pp. 1342–1351 (cit. on p. 22).

[45] H. Caswell. *Sensitivity analysis: matrix methods in demography and ecology*. Springer Nature, 2019 (cit. on p. 26).

[46] A. Saltelli et al. "Variance based sensitivity analysis of model output. Design and estimator for the total sensitivity index". In: *Computer physics communications* 181.2 (2010), pp. 259–270 (cit. on p. 26).

[47] I. M. Sobol'. "On sensitivity estimation for nonlinear mathematical models". In: *Matematicheskoe modelirovanie* 2.1 (1990), pp. 112–118 (cit. on p. 26).

[48] C. J. Stone. "The use of polynomial splines and their tensor products in multivariate function estimation". In: *The annals of statistics* (1994), pp. 118–171 (cit. on p. 26).

[49] S. IM and S. Kucherenko. "Global Sensitivity Indices for Nonlinear Mathematical Models. Review, vol. 1". In: *Wilmott* (2005), pp. 56–61 (cit. on p. 26).

[50] X. Yang et al. "Adaptive ANOVA decomposition of stochastic incompressible and compressible flows". In: *Journal of Computational Physics* 231.4 (2012), pp. 1587–1614 (cit. on p. 26).

[51] A. Saltelli et al. *Sensitivity analysis in practice: a guide to assessing scientific models*. Vol. 1. Wiley Online Library, 2004 (cit. on p. 28).

[52] O. Rakovec et al. "Distributed Evaluation of Local Sensitivity Analysis (DELSA), with application to hydrologic models". In: *Water Resources Research* 50.1 (2014), pp. 409–426 (cit. on p. 28).

[53] Y. Tang et al. "Comparing sensitivity analysis methods to advance lumped watershed model identification and evaluation". In: *Hydrology and Earth System Sciences* 11.2 (2007), pp. 793–817 (cit. on p. 28).

[54] N. A. Hamm, J. W. Hall, and M. Anderson. "Variance-based sensitivity analysis of the probability of hydrologically induced slope instability". In: *Computers & geosciences* 32.6 (2006), pp. 803–817 (cit. on p. 29).

[55] A. Saltelli et al. "Why so many published sensitivity analyses are false: A systematic review of sensitivity analysis practices". In: *Environmental modelling & software* 114 (2019), pp. 29–39 (cit. on p. 29).

[56] G. Casella and R. Berger. *Statistical inference*. CRC press, 2024 (cit. on p. 30).

[57] N. Metropolis et al. "Equation of state calculations by fast computing machines". In: *The journal of chemical physics* 21.6 (1953), pp. 1087–1092 (cit. on p. 31).

[58] J. Kaipio and E. Somersalo. *Statistical and computational inverse problems*. Vol. 160. Springer Science & Business Media, 2006 (cit. on p. 31).

[59] K. Ide et al. "Unified notation for data assimilation: Operational, sequential and variational (gtspecial issueltdata assimilation in meteology and oceanography: Theory and practice)". In: *Journal of the Meteorological Society of Japan. Ser. II* 75.1B (1997), pp. 181–189 (cit. on p. 31).

[60] J. Hadamard. *Lectures on Cauchy's problem in linear partial differential equations*. Courier Corporation, 2014 (cit. on p. 31).

[61] A. Quarteroni, A. Manzoni, C. Vergara, et al. *Mathematical modelling of the human cardiovascular system: data, numerical approximation, clinical applications*. Vol. 33. Cambridge University Press, 2019 (cit. on pp. 32, 54).

[62] R. Storn and K. Price. "Differential evolution–a simple and efficient heuristic for global optimization over continuous spaces". In: *Journal of global optimization* 11 (1997), pp. 341–359 (cit. on p. 32).

[63] R. Storn. "On the usage of differential evolution for function optimization". In: *Proceedings of North American fuzzy information processing*. Ieee. 1996, pp. 519–523 (cit. on p. 32).

[64] T. Bayes. "An essay towards solving a problem in the doctrine of chances". In: *Biometrika* 45.3-4 (1958), pp. 296–315 (cit. on p. 33).

[65] A. Perianes-Rodriguez, L. Waltman, and N. J. Van Eck. "Constructing bibliometric networks: A comparison between full and fractional counting". In: *Journal of informetrics* 10.4 (2016), pp. 1178–1195 (cit. on p. 36).

[66] R. C. Smith. *Uncertainty quantification: theory, implementation, and applications*. SIAM, 2024 (cit. on p. 36).

[67] J. M. Bardsley. "MCMC-based image reconstruction with uncertainty quantification". In: *SIAM Journal on Scientific Computing* 34.3 (2012), A1316–A1332 (cit. on p. 36).

[68] J. L. Mueller and S. Siltanen. *Linear and nonlinear inverse problems with practical applications*. SIAM, 2012 (cit. on p. 36).

[69] C. R. Vogel. *Computational methods for inverse problems*. SIAM, 2002 (cit. on p. 36).

[70] L. Mohamed, M. Christie, and V. Demyanov. "Comparison of stochastic sampling algorithms for uncertainty quantification". In: *SPE journal* 15.01 (2010), pp. 31–38 (cit. on p. 36).

[71] J. Zhang. "Modern Monte Carlo methods for efficient uncertainty quantification and propagation: A survey". In: *Wiley Interdisciplinary Reviews: Computational Statistics* 13.5 (2021), e1539 (cit. on p. 36).

[72] D. G. Cacuci, M. Ionescu-Bujor, and I. M. Navon. *Sensitivity and uncertainty analysis, volume II: applications to large-scale systems*. CRC press, 2005 (cit. on p. 36).

[73] N. Wiener. "The homogeneous chaos". In: *American Journal of Mathematics* 60.4 (1938), pp. 897–936 (cit. on p. 36).

[74] R. H. Cameron and W. T. Martin. "The orthogonal development of non-linear functionals in series of Fourier-Hermite functionals". In: *Annals of Mathematics* 48.2 (1947), pp. 385–392 (cit. on p. 36).

[75] W. Donders et al. "Personalization of models with many model parameters: an efficient sensitivity analysis approach". In: *International journal for numerical methods in biomedical engineering* 31.10 (2015) (cit. on p. 37).

[76] N. Toussaint et al. "In vivo human cardiac fibre architecture estimation using shape-based diffusion tensor processing". In: *Medical image analysis* 17.8 (2013), pp. 1243–1255 (cit. on p. 38).

[77] Z. Khalique et al. "Diffusion tensor cardiovascular magnetic resonance imaging: a clinical perspective". In: *Cardiovascular Imaging* 13.5 (2020), pp. 1235–1255 (cit. on p. 38).

[78] H. Wang et al. "Structure-based finite strain modelling of the human left ventricle in diastole". In: *International journal for numerical methods in biomedical engineering* 29.1 (2013), pp. 83–103 (cit. on p. 38).

[79] Y.-c. Fung. "A first course in continuum mechanics". In: *Englewood Cliffs* (1977) (cit. on p. 48).

[80] M. E. Gurtin. *An introduction to continuum mechanics*. Vol. 158. Academic press, 1982 (cit. on p. 48).

[81] L. E. Malvern. *Introduction to the Mechanics of a Continuous Medium*. Monograph. 1969 (cit. on p. 48).

[82] J. Bonet and R. D. Wood. *Nonlinear continuum mechanics for finite element analysis*. Cambridge university press, 1997 (cit. on pp. 48, 49, 54).

[83] M. Zeidi and C. I. Kim. "Mechanics of an elastic solid reinforced with bidirectional fiber in finite plane elastostatics: complete analysis". In: *Continuum Mechanics and Thermodynamics* 30.3 (2018), pp. 573–592 (cit. on p. 50).

[84] R. W. Ogden. *Non-linear elastic deformations*. Courier Corporation, 1997 (cit. on p. 50).

[85] A. Spencer. "Continuum Mechanics (Dover Books on Physics)". In: (2004) (cit. on p. 50).

[86] G. A. Holzapfel and N.-l. S. Mechanics. *A continuum approach for engineering*. 2000 (cit. on p. 50).

[87] W. Noll. "Lectures on the foundations of continuum mechanics and thermodynamics". In: *Archive for Rational Mechanics and Analysis* 52 (1973), pp. 62–92 (cit. on p. 52).

[88] C. Truesdell et al. *The non-linear field theories of mechanics*. Springer, 2004 (cit. on p. 52).

[89] D. Chapelle et al. "A poroelastic model valid in large strains with applications to perfusion in cardiac modeling". In: *Computational Mechanics* 46 (2010), pp. 91–101 (cit. on p. 54).

APPENDIX FOR CHAPTER 2

A.1 Constitutive Modelling of Passive Myocardium

The purpose of this section is to provide a mathematical description of the constitutive model used to characterize the mechanical behavior of the myocardium during passive diastolic filling. To this end, an overview of the fundamentals of soft tissue mechanics is presented, including the continuum mechanical framework, relevant kinematic and kinetic measures, and conservation laws. This is followed by a detailed discussion of hyperelastic modelling specific to cardiac tissue, including the role of fiber architecture and anisotropy, introduced in Section 2.1.3. Finally, the boundary value problem describing the system is provided.

A.1.1 Continuum Mechanics

Continuum mechanics is founded on the concept that a material (fluid, solid, or mixture) and its properties can be approximated by fields that are well defined almost everywhere [79–81]. This continuum assumption considers the scale at which discrete microstructural variations appear to much smaller than the smallest scales of interest. This enables the averaging of material characteristics, transforming the discrete nature of materials into well-defined point-wise fields. Conservation laws can be derived to enable computational simulations of heart tissue, detailing its movement, deformation (kinematics), and stress responses (kinetics). This section briefly reviews these concepts.

A.1.1.1 Kinematics of Large Deformation

Kinematics is the study of motion of particles or objects and its subsequent deformation without reference to the cause, i.e., without explicit consideration of the masses and forces involved [82]. To describe the motion of a body in a d-dimensional space, we define the region occupied by the body at $t = t_0$ as $\Omega_0 \subset \mathbb{R}^d$, to which we refer to as the *reference configuration*. The choice of a reference configuration is completely arbitrary[1].

---

[1]More generally, any configuration that the body is capable of occupying (irrespective of whether it actually does or not) may serve as a reference configuration.

Consequently, reference coordinates $\mathbf{X} \in \Omega_0$ describe the undeformed position of material particles within the body. In response to deformations, the material particles move to the coordinates $\mathbf{x} \in \Omega(t)$ at some time t, to which we refer to as the *current configuration*. Assuming that the reference coordinates, $\mathbf{X}$, and physical coordinates, $\mathbf{x}$, are related by a continuous displacement field $\mathbf{u}(\mathbf{X}, t)$, i.e., $\mathbf{x}(\mathbf{X}, t) = \mathbf{u}(\mathbf{X}, t) + \mathbf{X}$, we can then define the Jacobian of the mapping relative to the reference configuration, also known as the deformation gradient tensor, as

$$\mathbf{F} = \frac{\partial \mathbf{x}}{\partial \mathbf{X}} = \nabla_{\mathbf{X}} \mathbf{u} + \mathbf{I}, \tag{A.1}$$

where $\mathbf{I}$ is the identity tensor, with components described by the Kronecker delta symbol. For the description of local kinematics of any deformable body, we use the standard notation and convention

$$J = \det \mathbf{F} > 0. \tag{A.2}$$

Because J quantifies the local change in volume, then for an incompressible material, the constraint

$$J = \det \mathbf{F} \equiv 1 \tag{A.3}$$

must hold true.

The concepts of displacement field and deformation gradient are introduced to quantify the change in shape of infinitesimal line elements in a solid body [82]. To see this, let us draw a straight (red dashed) line on the undeformed configuration of a solid, as shown in Figure A.1.
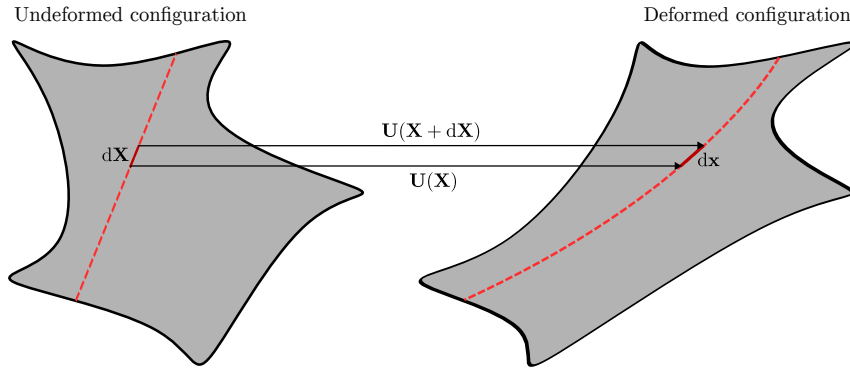

Figure A.1: Visualization of an infinitesimal line element in a deforming solid body. A reference straight line (dashed red) drawn on the undeformed configuration becomes a smooth curve upon deformation. However, a sufficiently small segment of this line, d$\mathbf{X}$, remains approximately straight after deformation, mapping to d$\mathbf{x}$ through the displacement field given by $\mathbf{u}(\mathbf{x} + d\mathbf{x}) - \mathbf{u}(\mathbf{x})$. This shows that despite global curvature, local material behavior can be captured by stretch and rotation only.

The line would be mapped to a smooth curve on the deformed configuration. However, suppose we focus on a line segment d$\mathbf{X}$, much shorter than the radius of curvature of this curve, as shown in Fig. A.1. The segment would be straight in the undeformed

configuration, and would also be (almost) straight in the deformed configuration. Thus, no matter how complex a deformation we impose on a solid, infinitesimal line segments are merely stretched and rotated by a deformation. We can then define the relation between infinitesimal line segments $d\mathbf{X}$ and $d\mathbf{x}$ as

$$d\mathbf{x} = \mathbf{F} \cdot d\mathbf{X}, \qquad dx_i = F_{ik} \cdot dX_k. \tag{A.4}$$

Following this logic, if a material fiber of initial length l_0 oriented along a unit vector $\mathbf{N}$ in the undeformed configuration, i.e. $d\mathbf{X} = l_0\mathbf{N}$, is stretched and rotated into a fiber of current length l and orientation $\mathbf{n}$ in the deformed configuration, i.e. $d\mathbf{x} = l\mathbf{n}$, then we can quantify the squared length of infinitesimal fibers in the deformed configuration through the deformation tensors as

$$||d\mathbf{x}||^2 = \frac{l^2}{l_0^2} = \mathbf{N} \cdot \mathbf{C} \cdot \mathbf{N}, \tag{A.5}$$

$$||d\mathbf{X}||^2 = \frac{l_0^2}{l^2} = \mathbf{n} \cdot \mathbf{B}^{-1} \cdot \mathbf{n}. \tag{A.6}$$

Here, $\mathbf{C}$ and $\mathbf{B}$ are the right and left Cauchy–Green deformation tensors, defined respectively as:

$$\mathbf{C} = \mathbf{F}^{\mathrm{T}} \cdot \mathbf{F}, \qquad C_{ij} = F_{ki} \cdot F_{kj}, \tag{A.7}$$

$$\mathbf{B} = \mathbf{F} \cdot \mathbf{F}^{\mathrm{T}}, \qquad B_{ij} = F_{ik} \cdot F_{jk}. \tag{A.8}$$

Both $\mathbf{C}$ and $\mathbf{B}$ are tensorial quantities used to model highly deformable solids such as the cardiac tissue and provide information about the local and directionally dependent stretch behavior of the material. Another commonly used kinematic quantity is the Green–Lagrange strain tensor, $\mathbf{E}$, that evaluates how much a given displacement differs locally from a rigid body displacement [83]:

$$\mathbf{E} = \frac{1}{2}(\mathbf{C} - \mathbf{I}), \qquad E_{ij} = \frac{1}{2}(C_{ij} - \delta_{ij}). \tag{A.9}$$

The development of a constitutive model requires coordinate independence and rigid body invariance [84, 85]. In order to account for those requirements, we define the principal invariants of $\mathbf{C}$ (and also of $\mathbf{B}$) as

$$I_1 = \mathrm{trace}\,(\mathbf{C}), \qquad I_2 = \frac{1}{2}[I_1^2 - \mathrm{trace}(\mathbf{C}^2)] \quad \text{and} \quad I_3 = \det \mathbf{C}, \tag{A.10}$$

where $I_3 = J^2 = 1$ for an incompressible material[2]. These invariants, however, model isotropic materials. Because the cardiac tissue is anisotropic, additional pseudo-invariants must be defined for directional dependence [86]. As explained in Section 2.1.3, the myocardium exhibits its greatest stiffness along the fiber direction $\mathbf{f}$, meaning we can model anisotropy under the assumption the material has a preferred direction in the

---

[2]The trace operator on $\mathbf{A} \in \mathbb{R}^{d \times d}$ is defined as $\mathrm{trace}\,(\mathbf{A}) = \sum_i A_{ii}$

reference configuration, from now on denoted by the unit vector $\mathbf{f}_0$. Therefore, two additional invariants can be defined as

$$I_4 = \mathbf{f}_0 \cdot (\mathbf{C}\mathbf{f}_0) \quad \text{and} \quad I_5 = \mathbf{f}_0 \cdot (\mathbf{C}^2\mathbf{f}_0). \tag{A.11}$$

Similarly, if there are two preferred directions, the second denoted by $\mathbf{s}_0$, then this introduces the invariants

$$I_6 = \mathbf{s}_0 \cdot (\mathbf{C}\mathbf{s}_0) \quad \text{and} \quad I_7 = \mathbf{s}_0 \cdot (\mathbf{C}^2\mathbf{s}_0). \tag{A.12}$$

Associated with it and, additionally, a coupling invariant, denoted by I_8, defined by

$$I_8 = \mathbf{f}_0 \cdot (\mathbf{C}\mathbf{s}_0) = \mathbf{s}_0 \cdot (\mathbf{C}\mathbf{f}_0). \tag{A.13}$$

Additionally, many models, including the one adopted in this work, consider splitting volumetric changes from distortional changes within the material. In this case, isochoric definitions of the deformation gradient are commonly used with corresponding changes to stretch tensors. In this case, we further decompose the deformation gradient $\mathbf{F}$ into volumetric ($\mathbf{F}_{\text{vol}}$) and isochoric ($\bar{\mathbf{F}}$) parts, as $\mathbf{F} = \bar{\mathbf{F}}\mathbf{F}_{\text{vol}}$ such that

$$\mathbf{F}_{\text{vol}} = J^{\frac{1}{3}}\mathbf{I} \quad \text{and} \quad \bar{\mathbf{F}} = J^{-\frac{1}{3}}\mathbf{F}, \tag{A.14}$$

leading to the definiton of the modified right Cauchy-Green tensor

$$\bar{\mathbf{C}} = \bar{\mathbf{F}}^{\text{T}}\bar{\mathbf{F}} = J^{-\frac{2}{3}}\mathbf{C}. \tag{A.15}$$

The reason for the decomposition of the deformation gradient $\mathbf{F}$ becomes clear once we introduce the constitutive law, particularly the strain energy function (See Section 2.2.1). Figure A.2 provides a visual overview of the deformation mechanism of a solid body under the assumptions made throughout this Section.
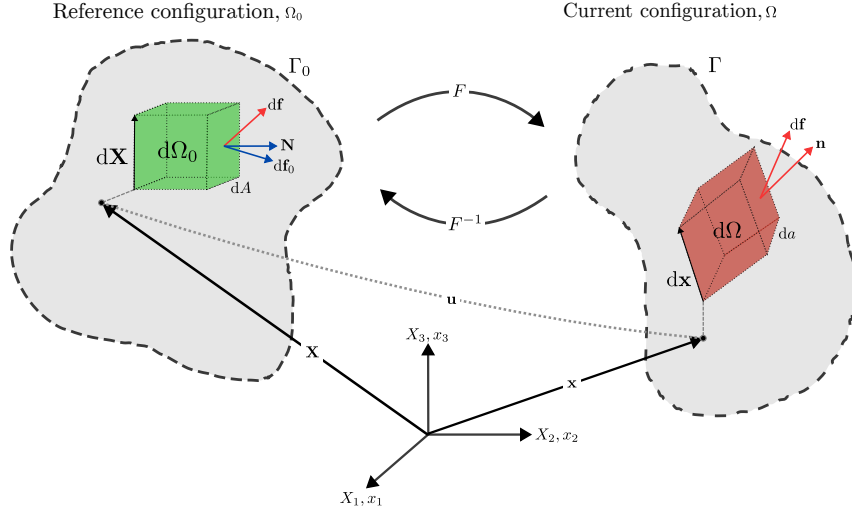
Figure A.2: General motion of a deformable body. The figure shows the mapping from a reference configuration (Ω_0, Γ_0), with material coordinates $\mathbf{X}_i$, to a deformed configuration (Ω, Γ), with spatial coordinates $\mathbf{x}_i$. The deformation gradient tensor $\mathbf{F}$ maps differential vectors $\mathrm{d}\mathbf{X}$ in the reference frame to $\mathrm{d}\mathbf{x}$ in the deformed frame, characterizing local changes due to deformation. Illustrated in the domain is also a differential volume element, representing the mapping of forces (reference, $\mathrm{d}\mathbf{f}_0$, and current, $\mathrm{d}\mathbf{f}$) along with normals (reference, $\mathbf{N}$, and current, $\mathbf{n}$) and areas (reference, $\mathrm{d}A$, and current, $\mathrm{d}a$).

A.1.1.2 Kinetics

Stress is a tensor variable that enables quantification of the internal tractions, meaning it describes the internal forces acting on a point in matter [28]. Cauchy postulated that a force on any surface that passes through a point depends only on its unit normal $\mathbf{n}$ [87]. To better understand the underlying mechanism of the Cauchy's stress theorem, let us consider a body $\mathscr{B}$ in the current configuration at a time t. In order to define the stress at some point P, let us further imagine a smooth surface Σ going through P and separating $\mathscr{B}$ into two parts (see Figure A.3). Following the classical mechanics framework of Newton and Euler [88], external forces applied on the body are transmitted internally via contact forces and moments, generating internal stresses across Σ.

On an element of area ΔS containing P, with the outward unit normal vector $\mathbf{n}$, the internal action of one side of the body on the other is characterized by a force $\Delta\mathbf{F}$ and, in general, a moment $\Delta\mathbf{M}$. For classical continua, the moment $\Delta\mathbf{M}$ is assumed to vanish. As the area shrinks to a point, Cauchy's postulate assumes that the limit

$$\lim_{\Delta S \to 0} \frac{\Delta\mathbf{F}}{\Delta S} \tag{A.16}$$

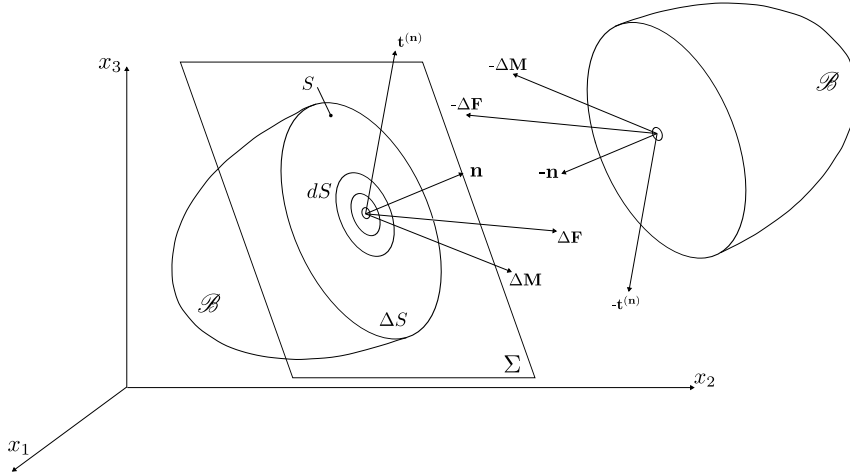exists and is finite, leading to the definition of the Cauchy traction vector $\mathbf{t}^{(\mathbf{n})}$.

Figure A.3: Illustration of Cauchy's stress theorem. A smooth internal surface Σ is introduced through a point P of the body $\mathscr{B}$ in its current configuration. The surface divides the body into two parts, allowing the definition of internal forces $\Delta\mathbf{f}$ and moments $\Delta\mathbf{m}$ exerted across the interface. According to Cauchy's postulate, the traction vector $\mathbf{t^{(n)}}$ acting on the surface element ΔS depends purely on the orientation of its unit normal vector $\mathbf{n}$ at P. Vectors on opposing sides of the body are shown with opposite signs to represent the balance of internal forces and moments, consistent with Cauchy's stress theorem and Newton's third law.

This traction vector $\mathbf{t^{(n)}}$ depends on both the spatial position and the orientation of the surface. According to Cauchy's postulate, the traction vector is the same for all surfaces through P that share the same normal vector $\mathbf{n}$. Therefore, it can be written as a linear mapping from the space of normal vectors to force vectors.

Provided that $\mathbf{t}$ is a continuous function of position $\mathbf{x}$, the mapping $\mathbf{n} \mapsto \mathbf{t}$ must be linear, and so we define the Cauchy stress tensor σ such that:

$$\mathbf{t^{(n)}} = \sigma \cdot \mathbf{n}, \qquad t_j^n = \sum_i \sigma_{ij} n_i. \tag{A.17}$$

This tensor σ characterizes the internal force distribution at a point in the current configuration of the body.

Depending on the orientation of the surface, the traction vector $\mathbf{t^{(n)}}$ may not be perpendicular to the plane on which it acts. Therefore, it can be decomposed into a normal component and a tangential component, defined respectively as

$$\sigma_n = \lim_{\Delta S \to 0} \frac{\Delta F_n}{\Delta S} = \frac{dF_n}{dS} \tag{A.18}$$

$$\tau_n = \lim_{\Delta S \to 0} \frac{\Delta F_s}{\Delta S} = \frac{dF_s}{dS}, \tag{A.19}$$

where dF_n is the component of force normal to the surface and dF_s is the component of force tangential to the surface.

By definition, the Cauchy stress is defined on the current configuration. However, the deformation gradient and strain tensors are described by relating the motion to the

reference configuration. Thus, not all tensors describing the state of the material are in either the reference or current configuration [82]. Describing the stress, strain and deformation either in the reference or current configuration would make it easier to define constitutive models. To bypass this limitation, one can construct equivalent quantities to express the stress relative to the reference configuration. These are known as the first and second Piola–Kirchhoff stresses. The first Piola–Kirchhoff stress tensor, denoted by $\mathbf{P}$, satisfies $\frac{d\mathbf{f}}{dA} = \mathbf{PN}$ for all surfaces passing through the point on the reference configuration with normal $\mathbf{N}$ and surface area dA. Since $\mathbf{N}$ and dA are often more easily measured at the beginning of experiments, this form of stress can be more practical. $\mathbf{P}$ can be defined as

$$\mathbf{P} = J\sigma\mathbf{F}^{-T}. \tag{A.20}$$

Because the first Piola–Kirchhoff $\mathbf{P}$ stress tensor relates forces in the current configuration with areas in the reference configuration, relating different coordinate systems, it is not symmetric. Alternatively, the second Piola–Kirchhoff stress tensor, $\mathbf{S}$, relates forces in the reference configuration to areas in the reference configuration. Therefore,

$$\mathbf{S} = J\mathbf{F}^{-1}\sigma\mathbf{F}^{-T} \tag{A.21}$$

is a symmetric tensor. Since the relations are defined within the same configuration ($d\Omega_0$), $\mathbf{S}$ is a convenient quantity for constitutive modelling.

A.1.1.3 Conservation Laws

To complete the mechanical description of deformable solids such as cardiac tissue, it is necessary to impose the physical conservation laws of mass and momentum [28, 61, 89]. The conservation of mass states that the mass of a body in a closed system can only be created or destroyed by a known source, which means we can assume that the material density is preserved as the myocardium deforms. It is written in the reference configuration as

$$\frac{D\rho J}{Dt} = \hat{\rho}J, \tag{A.22}$$

which states that the rate of change in mass, ρJ, is equal to the rate of mass being generated by a source $\hat{\rho}$. Here, $\frac{D}{Dt} = \frac{\partial}{\partial t} + \mathbf{v} \cdot \nabla$ defines the Lagrangian time derivative. For incompressible materials with constant density and no source of growth, the remaining mass balance equation is equivalent to $J - 1 = 0, \forall \mathbf{X} \in \Omega_0$.

Under the conditions of negligible acceleration and no body forces, the conservation of linear momentum simplifies to the null divergence of the first Piola–Kirchhoff stress tensor $\mathbf{P}$:

$$\mathrm{Div}\,\mathbf{P} = \mathbf{0}, \quad \forall \mathbf{X} \in \Omega_0. \tag{A.23}$$

This condition removes any dependency from the current configuration by forcing mechanical equilibrium in the reference configuration, and forms the foundation of the finite element formulation adopted in this work.

Finally, for completeness, the conservation of angular momentum states that the angular momentum of an isolated body remains constant in the absence of external forces. This translates to the requirement that the Cauchy stress tensor σ must remain symmetric under equilibrium conditions. In the current work, this is naturally satisfied through the use of the symmetric Cauchy stress tensor σ.